Approach for propagating radiometric data uncertainties through NASA ocean color algorithms

Lachlan I.W. McKinna[1,*], Ivona Cetinić[2,4], Alison P. Chase[3], P. Jeremy Werdell[4]

[1]Go2Q Pty Ltd, Sunshine Coast, QLD, Australia

[2]GESTAR/Universities Space Research Association, Columbia, MD, USA

[3]School of Marine Sciences, University of Maine, Orono, ME, USA

[4]NASA Goddard Spaceflight Center, Code 616, Greenbelt, MD

*** Correspondence:**
Lachlan I.W. McKinna
lachlan.mckinna@go2q.com.au

Keywords: Ocean color, remote sensing, bio-optics, uncertainties

Abstract

Spectroradiometric satellite observations of the ocean are commonly referred to as "ocean color" remote sensing. NASA has continuously collected, processed, and distributed ocean color datasets since the launch of the Sea-viewing Wide-field-of-view Sensor (SeaWiFS) in 1997. While numerous ocean color algorithms have been developed in the past two decades that derive geophysical data products from sensor-observed radiometry, few papers have clearly demonstrated how to estimate measurement uncertainty in derived data products. As the uptake of ocean color data products continues to grow with the launch of new and advanced sensors, it is critical that pixel-by-pixel data product uncertainties are estimated during routine data processing. Knowledge of uncertainties can be used when studying long-term climate records, or to assist in the development and performance appraisal of bio-optical algorithms. In this method paper we provide a comprehensive overview of how to formulate first-order first-moment (FOFM) calculus for propagating radiometric uncertainties through a selection of bio-optical models. We demonstrate FOFM uncertainty formulations for the following NASA ocean color data products: chlorophyll-a pigment concentration (*Chl*), the diffuse attenuation coefficient at 490 nm ($K_{d,490}$), particulate organic carbon (*POC*), normalized fluorescent line height (*nflh*), and inherent optical properties (IOPs). Using a quality-controlled *in situ* hyperspectral remote sensing reflectance ($R_{rs,i}$) dataset, we show how computationally inexpensive, yet algebraically complex, FOFM calculations may be evaluated for correctness using the more computationally expensive Monte Carlo approach. We compare bio-optical product uncertainties derived using our test R_{rs} dataset assuming spectrally-flat, uncorrelated relative uncertainties of 1, 5, and 10%. We also consider spectrally dependent, uncorrelated relative uncertainties in R_{rs}. The importance of considering spectral covariances in R_{rs}, where practicable, in the FOFM methodology is highlighted with an example SeaWiFS image. We also present a brief case study of two *POC* algorithms to illustrate how FOFM formulations may be used to construct measurement uncertainty budgets for ecologically-relevant data products. Such knowledge, even if rudimentary, may provide useful information to end-users when selecting data products or when developing their own algorithms.

1 Introduction

NASA has continually collected, processed, archived, and distributed global ocean color data since the launch of the Sea-viewing Wide Field-of-View Sensor (SeaWiFS) in 1997. This two decades-long multi-sensor data climatology continues to provide unprecedented synoptic-scale insight into near-surface oceanographic processes. Some of the satellite-derived variables, such as chlorophyll-a pigment concentration *Chl* (mg m^{-3}), are considered as Essential Climate Variables (ECV) and are widely used by the oceanographic community to study phytoplankton ecology, marine biogeochemistry, and ecosystem responses to climate change (Franz et al., 2017; IOCCG, 2008; McClain, 2009).

Following formal definitions outlined in the Guide to Uncertainty in Measurement (JCGM, 2008), we can consider the objective of ocean color remote sensing is to *measure* oceanographic quantities or *measurands*. We note that the *measurement procedure* involves a number of mathematical steps and assumptions that derive the *measurand* from sensor-observed top-of-atmosphere radiances. Thus, a derived ocean color data product is a *result of measurement* and should always be treated as an estimate of the *measurand* which has inherent *uncertainty*.

Quantifying uncertainty in derived ocean color data products (i.e. measurands) is highly valuable, allowing end-users to: assess if datasets are fit-for-purpose, assess if observed temporal change is greater than uncertainty, assimilate uncertainties into climate models, and assess consistency among sensors (Gould et al., 2014; Maritorena et al., 2010). Additionally, a thorough understanding of uncertainty sources within a model can help guide the decisions of scientists when developing new satellite algorithms.

The measurement uncertainty, ($u_{measurement}$), in an ocean color data product, y, can be expressed as the following:

$$u_{measurement}(y) = \sqrt{u^2_{data}(y) + u^2_{model}(y)} \,, \tag{1}$$

where $u_{model}(y)$ represents uncertainties in y due to inherent inaccuracies/limitation in the algorithm (e.g. model coefficients), and $u_{data}(y)$ represents uncertainties in y due to uncertainties in sensor-observed radiometry (data). In this paper we focus on u_{data}(y), that is, the propagation of radiometric uncertainties through bio-optical algorithms. For brevity, we shorten $u_{data}(y)$ to $u(y)$ throughout this paper unless otherwise stated.

For the ocean color community, much of our understanding of measurement uncertainty in derived data products is sourced from validation exercises using *in situ* datasets (Antoine et al., 2008; Bailey & Werdell, 2006; Melin, 2010; Mélin et al., 2016) or from Monte Carlo-type simulations (Wang et al., 2005). We note that advanced statistical methodologies have also emerged for predicting uncertainties in derived ocean color products (Jay et al., 2018; Moore et al., 2009; Salama et al., 2009). While validation studies remain critical for appraising the absolute skill of an ocean color algorithm, such datasets themselves have their own measurement uncertainty associated with *in situ* observations (including uncertainties associated with subpixel temporal/spatial/environmental variability). Monte Carlo-type analyses are particularly useful for understanding measurment uncertainty, however, these approaches can be computationally expensive and are impracticable to implement within pixel-by-pixel ocean color processing.

More recently, analytical first-order first moment (FOFM) methods have been proposed that can directly propagate radiometric uncertainty through an ocean color algorithm to estimate derived data product uncertainty (Lamquin et al., 2013; Lee et al., 2010; Maritorena et al., 2010; Neukermans et al., 2009; Qi et al., 2017; Salama et al., 2009; Salama et al., 2011). These approaches are based on the *law of propagation of uncertainty* according to JCGM (2008). A FOFM methodology benefits from being computationally efficient, thereby allowing it to be implemented in pixel-by-pixel ocean color data processing software (Lamquin et al., 2013). In addition, FOFM calculations can be used to estimate the relative contribution of individual sources to total measurement uncertainty.

Work presented here is the first comprehensive examination of methods that can be used to estimate uncertainties in NASA's standard bio-optical data products. In this study we aim to demonstrate the feasibility of using a FOFM uncertainty framework to approximate ocean color data uncertainty in derived data products. The FOFM method, which itself is an analytical approximation, is first appraised by comparing FOFM-derived uncertainties with Monte Carlo-derived uncertainties. We demonstrate how this approach can be used as a method to check the correctness of FOFM calculations. Second, using FOFM propagation theory, we estimate uncertainty in derived ocean color products given spectrally-flat, uncorrleated relative uncertainties of 1, 5, and 10% in spectral remote-sensing reflectances, $R_{rs,i}$ (sr^{-1}). We also consider spectrally dependent uncorrelated, relative uncertainties in $R_{rs,i}$ published by Hu et al. (2013). Third, we consider how inclusion of covariances affect uncertainties estimates. A sample SeaWiFS scene of the Hawaiian Islands is used in this case study. Finally, we demonstrate how the FOFM approach may be used to estimate measurement uncertainty budgets. In our case study we consider two algorithms used to estimate particulate organic carbon (*POC*; mg m^{-3}), a key metric used to understand oceanic biomass and the carbon cycle.

In this work, we utilize a high quality *in situ* hyperspectral $R_{rs,i}$ dataset that can be spectrally subsampled to match the spectral characteristics of most existing and future ocean color sensors. This includes NASA's Plankton, Aerosol, Cloud, ocean Ecosystem (PACE) mission that is currently under development and will carry the first dedicated hyperspectral ocean color sensor.

2 Data and methods

2.1 Bio-optical algorithms and data products

The NASA Ocean Biology Data Archive and Active Distribution Center (OB.DAAC) distribute a number of derived marine data products in two separate data suites: (i) the standard ocean color (OC) data product suite and, (ii) the inherent optical properties (IOP) product suite. The OC suite comprises established (legacy) ocean color data products that were developed during the SeaWiFS` (1997 – 2010) and Moderate Resolution Imaging Spectroradiometer aboard Aqua (MODISA 2002 – present) missions. The IOP suite comprises spectral component absorption and backscattering coefficients derived using the default configuration of the Generalized Inherent Optical Properties (GIOP) algorithm framework (Werdell et al., 2013). A selection of the OC suite and IOP suite products were used in this study (Table 1). More comprehensive detail of the bio-optical algorithms used to derive these data products and their associated uncertainties are given in Appendices A-E. We note that in this study the GIOP used a spectral subset of our R_{rs} evaluation dataset (described in section 2.3) spanning 412 – 655 nm.

2.2 Modelling bio-optical data product uncertainty

In this study we used the analytical law of propagation of uncertainty (JCGM, 2008) to propagate radiometric uncertainties through models used to derive bio-optical quantities. We follow the notation conventions outlined by JCGM (2008) where the uncertainty of a measured quantity, y, is denoted as $u(y)$ and is the positive square root of the variance, $u^2(y)$. We note that y is derived from a model, f, of N input quantities, x_i. Following (JCGM, 2008), for uncorrelated input quantities, $u^2(y)$ can be calculated as:

$$u^2(y) = \sum_{i=1}^{N} \left(\frac{\partial f}{\partial x_i} \right)^2 u^2(x_i) \tag{2}$$

where, $u(x_i)$ is the 1-σ uncertainty in the input quantity x_i. For our notation of spectral properties used in ocean color remote sensing, subscripts i correspond to wavelength. In this study, partial derivatives of target parameters were calculated analytically, however, these could also be computed numerically. For the situation where uncertainties of input quantities are correlated, Equation 2 is extended to:

$$u^2(y) = \sum_{i=1}^{N} \left(\frac{\partial f}{\partial x_i} \right)^2 u^2(x_i) + 2\sum_{i=1}^{N-1} \sum_{j=i+1}^{N} \frac{\partial f}{x_i} \frac{\partial f}{x_j} u(x_i, x_j) \tag{3}$$

where $u(x_i, x_j) = u(x_j, x_i)$ denotes the estimated error covariance associated with the quantities x_i and x_j. Comprehensive details of partial derivative calculations for each bio-optical algorithm in Table 1 are given in Appendices A-E.

Monte Carlo (MC) methods are routinely used to perform sensitivity analyses as well as quantify model output uncertainties (Refsgaard et al., 2007). In this study, we have utilized a MC approach to appraise FOFM calculations. As the partial derivative calculus within FOFM uncertainty estimates can be complex, we have used MC-to-FOFM comparisons as a means of checking calculations.

The MC estimates of uncertainties in this study were computed as follows:

(i) A given bio-optical model, f, that derives an output y, that is considered a function of n spectral remote sensing reflectance bands, $R_{rs,i}$, is run 5,000 times.

(ii) Upon each iteration, each $R_{rs,i}$ is perturbed by a factor $\Delta r_{,i}$ which is randomly sampled from a Gaussian distribution $\Delta r_{,i} \sim N(0, u(R_{rs,i}))$, in which the mean is zero and the standard deviation, $u(R_{rs,i})$, is known or assumed. No spectral correlations are assumed.

(iii) The MC simulation then generates a probability density function (*PDF*) for y. From the *PDF*, the mean value, $\hat{y}$, and the standard deviation, s_y, can be computed.

We note that the MC method captures non-linear affects and thus we cannot always expect direct agreement between s_y^2 and FOFM-derived $u^2(y)$. Indeed, even if a bio-optical model contains weak nonlinearities and MC model input uncertainties are normally distributed, the number of MC iterations still needs to be suitably large for s_y^2 to agree with $u^2(y)$.

2.3 Evaluation R_{rs} dataset

To evaluate our FOFM uncertainty method, we used a dataset of high quality hyperspectral $R_{rs,i}$ spectra (N=1124). Hyperspectral radiometric measurements were collected *in situ* during three different expeditions, representing a range of oligotrophic to mesotrophic waters: the SABOR experiment in the Gulf of Maine/North Atlantic/Mid-Atlantic coast (July–August 2014); AE1319 in the North Atlantic and Labrador Sea (August–September 2013); and NH1418 in the Equatorial Pacific (September–October 2014). A HyperOCR system (Sea-Bird Scientific) deployed on a tethered profiler in "buoy mode" was used to collect upwelling radiance, $L_{\mathrm{u,i}}$ (W m^{-2} μm^{-1} sr^{-1}), and downwelling irradiance, $E_{\mathrm{d,i}}$ (W m^{-2}), spectra during deployments lasting approximately five minutes. During sample collection, the instrument was allowed to drift far enough from the boat to avoid the ship's shadow.

The spectra were dark and tilt-corrected, and the upper and lower 25$^{\mathrm{th}}$ percentile of the $E_{\mathrm{d,i}}$ spectra were removed from both $E_{\mathrm{d,i}}$ and $L_{\mathrm{u,i}}$. The mean of the remaining spectra was used in subsequent analysis, providing one spectrum per deployment, and with uncertainties calculated as the standard deviation of the same spectra used to calculate the mean (N.B. uncertainties here represent only the experimental portion of the uncertainties, and calibration bias has not been accounted for). The $L_{\mathrm{u,i}}$ measurements were extrapolated to and across the air-water interface to obtain the water-leaving radiance, $L_{\mathrm{w,i}}$ (W m^{-2} sr^{-1}), which were then used to calculate remote-sensing reflectance ($R_{\mathrm{rs,i}}$), defined as:

$$R_{rs,i} = \frac{L_{w,i}}{E_{d,i}} \tag{4}$$

The spectra were additionally corrected for Raman scattering following methods in Westberry et al. (2013), which was necessary to compensate for the scattering that water molecules themselves can contribute to $L_{\mathrm{w,i}}$, especially at the blue wavelengths in very clear waters (McKinna et al., 2016). Finally, the R_{rs} spectra were normalized to remove the angular effect of the sun position in the sky relative to nadir, following methods in Lee et al. (2011). For a more detailed description of the $R_{\mathrm{rs,i}}$ calculations and processing, see Data and Methods section in Chase et al. (2017). All hyperspectral $R_{rs,i}$ used in this study are shown in Figure 1.

Finally, each hyperspectral R_{rs} spectrum was spectrally sub-sampled. The resulting multiband $R_{\mathrm{rs,i}}$ dataset had sixteen 10 nm-wide spectral bands centered on: 412, 425, 443, 460, 475, 490, 510, 532, 555, 583, 617, 640, 655, 665, 678, 710 nm. This multispectral subset spanned the visible domain and included bands from both past and present NASA sensors (e.g. SeaWiFS and MODIS).

2.4 Radiometric uncertainties

2.4.1 Spectrally flat R_{rs} uncertainties

For NASA ocean color bio-optical algorithms, model input quantities are typically remote sensing reflectances, $R_{rs,i}$ (sr^{-1}), which are derived from measured top-of-atmosphere radiances, $L_{t,i}$ (W m^{-2} μm^{-1} sr^{-1}), via atmospheric correction (AC) algorithms. Historically, a desirable science requirements for NASA ocean color missions has been $R_{rs,i}$ with relative uncertainty of 5% (spectrally flat) or less (Hooker et al., 1992; Hooker & McClain, 2000; McClain et al., 2004; PACE Science Definition Team, 2018). Whilst not directly representative of a true sensor (see section 2.4.2), treating relative uncertainties in $R_{rs,i}$ as spectrally flat is still useful under circumstances where detailed knowledge of sensor performance characteristics is limited, such as during pre-launch scoping studies, to provide rudimentary uncertainty estimates. In this study we first consider 5% relative uncertainty in $R_{rs,i}$ to compare FOFM-to-MC calculations. We next use the FOFM method consider how spectrally flat relative uncertainties in R_{rs} of 1, 5, and 10% impact estimated OC and IOP uncertainties. Note, we treat spectrally flat relative uncertainties in R_{rs} of 1, 5, and 10% as spectrally uncorrelated.

2.4.2 Spectrally-dependent R_{rs} uncertainties

We note that on-orbit uncertainties in $L_{t,i}$ and $R_{rs,i}$ have previously been quantified for NASA's SeaWiFS and MODISA missions (Angal et al., 2015; Eplee et al., 2007; Hu et al., 2013; Hu, Feng, et al., 2012). Whilst historically 5% has been the desired accuracy goal for R_{rs} in the blue-green spectral range, work by Hu et al. (2013) reported that relative uncertainties of $R_{rs,i}$ for SeaWiFS and MODISA increase monotonically with wavelength, and that $R_{rs,i}$ relative uncertainty also varies as a function of *Chl*, or water-column optical complexity. To extend this study beyond spectrally flat relative uncertainties, we utilized the relative uncertainties for MODISA $R_{rs,i}$ estimated for the North Atlantic Ocean (see Table 2 of Hu et al. (2013)). To estimate relative uncertainty for a given $R_{rs,i}$ spectra, we followed three steps: (i) linearly interpolate tabulated relative uncertainties to match the spectral resolution of our in situ $R_{rs,i}$ dataset, (ii) estimate *Chl* concentration using NASA's standard OC algorithm, and (iii) linearly interpolate the spectrally tabulated relative uncertainties to estimate relative uncertainty for observed $R_{rs,i}$ based on the respective *Chl* concentration. Note, where estimated *Chl* exceeded 0.2 mg m^{-3} (beyond values reported by Hu et al. (2013)), we linearly extrapolated tabulated relative uncertainties. Figure 2 shows the spectral relative uncertainties in $R_{rs,i}$ (*sensu* Hu et al. (2013)) used in this study and how they vary with *Chl* concentration. Note, spectrally-dependent relative uncertainties in R_{rs} computed as a function of *Chl* were treated as spectrally uncorrelated.

2.4.3 Spectrally-correlated R_{rs} uncertainties

Our initial analyses treated R_{rs} spectral uncertainties as uncorrelated, which in practice is an oversimplification. Indeed, AC algorithms utilize near-infrared bands to make assumption about the contribution of atmospheric aerosols to L_t (Bailey et al., 2010; Gordon & Wang, 1994). Thus, $R_{rs,i}$ uncertainties are inherently spectrally correlated. While much work has been done to characterize radiometric uncertainties of NASA sensors used for ocean color (Eplee et al., 2007; Hu et al., 2013; Hu, Feng, et al., 2012), few studies have quantified off-diagonal elements of the variance-covariance matrices for top-of-atmosphere radiance, $\mathbf{V}_{Lt}$, and remote sensing reflectances, $\mathbf{V}_{Rrs}$, respectively. We note that while beyond the scope of this work, parallel efforts are underway by the research community to derive pixel-by-pixel estimates of $u(R_{rs,i})$ by propagating radiometric uncertainties through ocean color atmospheric correction algorithms (Gillis et al., 2018).

Recently, Lamquin et al. (2013) demonstrated a methodology to estimate $\mathbf{V}_{Lt}$, for MERIS data and propagate these through ESA's clear water branch AC algorithm and into bio-optical data products. Critically, Lamquin et al. (2013) demonstrated that ignoring covariances can lead to overestimated data product uncertainties. In this study, using a similar methodology to Lamquin et al. (2013) we estimate $\mathbf{V}_{Lt}$ for SeaWiFS and then using a numerical approximation estimate $\mathbf{V}_{Rrs}$. A full description of this method can be found in Appendix F. We note that while our estimates of $\mathbf{V}_{Rrs}$ are somewhat rudimentary, they are still useful for demonstrating the importance of including covariance terms in FOFM-based uncertainty estimates.

2.5 Satellite data processing

A SeaWiFS image of Hawaii captured on 1 December 2000 was used to demonstrate the FOFM methodology when applied to ocean color imagery. SeaWiFS Level-1 data was downloaded from NASA's Ocean Biology Distributed Active Archive Center (OB.DAAC) Level 1 and 2 Browser website (https://oceancolor.gsfc.nasa.gov/). Data were then processed from Level 1 to Level 2 using NASA Ocean Color Science Software (OCSSW). These processing steps include radiometric calibration, geolocation, and atmospheric correction. A prototype version of OCSSW code was used to compute $u(Chl)$ using FOFM methodology where $u(R_{rs,i})$ was estimated using an empirical methodology described in Appendix F.

3 Results

3.1 Appraisal of methodology

The MC methodology, while computationally expensive, was expected to give robust estimates of measurand uncertainties. Thus, MC outputs provided a benchmark to which the FOFM uncertainty estimates could be compared with for correctness. Direct calculations of FOFM uncertainties, $u(y)$, were compared with MC output uncertainties, s_y. To compare MC and FOFM calculations we used 5% spectrally flat relative uncertainty in R_{rs} and computed the following comparison statistics: bias, and Type II linear regression slope. When computing these statistics for the purpose of FOFM-to-MC comparisons, we assume that MC-estimated uncertainties were quasi-truth. We note that variables were log-transformed for these calculations following Seegers et al. (2018). Bias was computed as:

$$bias = 10 \wedge \left\{ \sum_{k=1}^{N} \frac{\log_{10}(MC_k) - \log_{10}(FOFM_k)}{N} \right\}, \qquad (5)$$

where N=1124 is the number of input spectra. Given that bias was computed using log-transformed variables, it becomes interpretable as multiplicative metrics (Seegers et al., 2018). We note that our bias calculations assume estimated OC and IOP uncertainties follow log-normal distributions; a property that is demonstrated later in the paper (e.g. Figures 5 and 6).

The MC and FOFM estimation of derived product uncertainties were in good agreement for the following OC products: $K_{d,490}$, *POC*, and *nflh*. This was indicated by slope and bias and statistics (Table 2) having values of, or near to, 1.0. However, regression statistics indicated *Chl* uncertainties derived using the FOFM method did not completely agree with the MC method (Table 2). To assess this discrepancy closer, uncertainties in each component of the *Chl* algorithm were inspected, namely the band ratio (BR), line height (LH), and blended components. Regression statistics indicated that FOFM estimates of Chl_{blend} product uncertainties did not agree well with MC values and were typically biased low by 29%, visualized further by the color-coded scatter plot in Figure 3a.

Derived uncertainties for IOP products generally agreed with MC simulations. Specifically, Table 2 shows FOFM estimates of uncertainties with respect to MC estimates for $a_{nw,443}$, $a_{\phi,443}$, $a_{dg,443}$, and $b_{bp,443}$ were biased low by 1%, low by 2%, low by 2% and, high by 2%, respectively. Slight disagreement between MC and FOFM estimates of $u(b_{bp,443})$ can be visualized in Figure 3 when $u(b_{bp,443}) > 2.0\text{x}10^{-3}$ m^{-1}. In addition, MC and FOFM estimates of $u(a_{\phi,443})$ showed slight disagreement when $u(a_{\phi,443}) > 1.0\text{x}10^{-2}$ m^{-1}.

These results demonstrate that while FOFM uncertainty calculations are computationally inexpensive, they serve as approximations only, especially in the case of *Chl*. Indeed, while FOFM-derived uncertainties can be expected to agree with MC-derived values for simple functions that vary linearly, it may not be unusual for FOFM-derived uncertainties to differ from MC-derived values; particularly when analyzing complicated non-linear problems (Mekid & Vaja, 2008; Putko et al., 2001). For example, with the IOPs we found slight differences in the order of 1% between MC and FOFM uncertainty estimates. For such mathematical functions, higher order methods such as Second Order

First Moment (SOFM) methods may be useful, however, the added mathematical complexity may be prohibitive.

3.2 Uncertainties estimated from *in situ* radiometric data

3.2.1 OC product uncertainties

Using the multispectral R_{rs} evaluation dataset, uncertainties in derived OC products associated with 5% spectrally-flat relative, uncorrelated uncertainty in R_{rs} were computed. Figure 4 shows histograms of derived OC products, absolute uncertainties, and relative uncertainties. MC computations are summarized in Table 3 while FOFM computations are provided for comparative purposes in Table 4.

The range of derived *Chl* confirmed that the dataset spans oligotrophic (0.04 mg m^{-3}) to mesotrophic conditions (1.28 mg m^{-3}) with a median value of 0.11 mg m^{-3}. Values of $u(Chl)$ span four orders of magnitude and have median values of 7.00x10^{-3} mg m^{-3} and 6.70x10^{-3} mg m^{-3} for the MC and FOFM methods, respectively. The relative uncertainties for *Chl* span a single order of magnitude and have a median values of 9.74% and 9.67% for the MC and FOFM methods, respectively. Although the histogram of derived *Chl* in Figure 4 appears log-normally distributed, two distinct peaks are present; a low peak (ranging from 0 – 0.5 mg m^{-3}) and a high peak (centered on 1.1 mg m^{-3}). Since bio-optical properties are log-normally distributed in the ocean (Campbell, 1995), the peaks observed in the distributions of derived bio-optical variables are probably due to the limited size of the hyperspectral R_{rs} dataset (N=1124), that does not uniformly span the entire range of oceanic conditions (see Fig 1A in Chase et al. (2017))

The range of derived $K_{d,490}$ spans an order of magnitude with a median value of 0.0291 m^{-1}. The values of $u(K_{d,490})$ also span an order of magnitude with median values of 2.68x10^{-3} m^{-1} for both MC and FOFM calculations. The relative uncertainties for $K_{d,490}$ span a single order of magnitude and have a median value of 8.94% and 8.91% for MC and FOFM calculations, respectively. The range of derived *POC*, spans two orders of magnitude with a median value of 33.1 mg m^{-3}. The values of $u(POC)$ span an order of magnitude and have median values of 2.44 mg m^{-3} and 2.42 mg m^{-3} for MC and FOFM calculations, respectively. The relative uncertainties in *POC* have a of value of 7.37% and 7.31% for MC and FOFM calculations, respectively. We note that the relative uncertainty in *POC* as computed by FOFM method exhibits no spread. For uncorrelated, spectrally flat relative uncertainties, $u(POC)/POC$ is a function of $u(Rrs,_{443})/R_{rs,443}$ and $u(Rrs,_{555})/R_{rs,555}$. Thus, when $u(Rrs,_{443})/R_{rs,443}$ and $u(Rrs,_{555})/R_{rs,555}$ is fixed (e.g. at 5%), $u(POC)/POC$ are fixed. In practice, this will not always hold true, particularly when relative uncertainties in R_{rs} are variable and spectrally dependent. We note that in Figure 4 the MC-derived relative uncertainties for *POC* are normally distributed over a narrow range centered on 7.37%.

The range of *nflh* spans three orders of magnitude with an MC-estimated median value of 2.20x10^{-3} mW cm^{-2} µm^{-1} sr^{-1}. We note that direct calculations of *nflh* resulted in a median value of 2.19x10^{-3} mW cm^{-2} µm^{-1} sr^{-1}. The values of $u(nflh)$ span an order of magnitude with median values of 9.86x10^{-4} mW cm^{-2} µm^{-1} sr^{-1} and 9.87x10^{-4} mW cm^{-2} µm^{-1} sr^{-1} for MC and FOFM calculations, respectively. The median relative uncertainty in *nflh* was 41.9% and 42.1% for MC and FOFM calculations, respectively (Figure 4). We note that the range of relative errors for *nflh* is very large (for MC calculations: 14.8 – 1.7 x10^{4} %), and these should be interpreted with a caution. Low values of *nflh*, in the order of 1x10^{-6} mW cm^{-2} µm^{-1} sr^{-1}, were derived from the evaluation dataset which in most likelihood would be beyond the detection limit of existing ocean color sensors. Further, while the absolute uncertainties associated with these low *nflh* value may also be small in magnitude, they can still manifest as large relative errors.

3.2.2 IOP product uncertainties

Using the radiometric evaluation dataset, uncertainties in derived IOP products associated with 5% relative, uncorrelated uncertainty in $R_{rs,i}$ were computed following the methodology in Appendix E. Figure 5 shows histograms of derived IOP products, absolute uncertainties, and relative uncertainties. MC computations are summarized in Table 5 while FOFM computations are provided for comparative purposes in Table 6.

The range of derived $a_{nw,443}$ spans two orders of magnitude with a median value of 0.0185 m^{-1}. Values of $u(a_{nw,443})$ span an order of magnitude with median values of $2.31x10^{-3}$ m^{-1} and $2.26x10^{-3}$ m^{-1} for MC and FOFM methods, respectively. The median relative uncertainty in $a_{nw,443}$ spans a single order of magnitude and has median values of 12.6% and 12.2% for MC and FOFM methods, respectively. The range of $a_{\phi,443}$, $a_{dg,443}$, and $b_{bp,443}$ all span a single order of magnitude with median values of $9.6x10^{-3}$ m^{-1}, $8.71x10^{-3}$ m^{-1}, and $1.08x10^{-3}$ m^{-1}, respectively. Absolute uncertainties in IOPs all span two orders of magnitude apart from $u(a_{\phi,443})$ which spanned a single order of magnitude. Highest relative uncertainties of all GIOP-derived products are for $a_{\phi,443}$ (~ 20%), whereas $a_{nw,440}$, $a_{dg,440}$, and $b_{bp,440}$ have relative uncertainties of similar magnitude that are all less than 15%.

3.2.3 Summary of MC and FOFM comparisons

FOFM and MC estimates of OC and IOP uncertainties were generally in good agreement. This provides confidence that our FOFM analytical formulations were correct. However, FOFM-to-MC comparisons of *Chl* and IOP uncertainties, whilst similar in magnitude, exhibited a degree of scatter around the one-to-one line. We expect that these differences may be due to the MC method's ability to handle non-linearity and discontinuities in the models more robustly than the FOFM approach. For example, the *Chl* model has several complex features such: switching between Chl_{BR} *and* Chl_{LH}, the Chl_{BR} model's selection of maximum band ratios, and the blending of Chl_{BR} *and* Chl_{LH} which may not be fully captured by the FOFM method.

We thus found FOFM-to-MC comparisons to be useful as a "quick acceptability checking" of FOFM calculations. In practice, however, one should not always assume the two methods will closely agree as the MC model may handle non-linearities and discontinuities more robustly than the FOFM method. The FOFM and MC calculations also indicate that for normally distributed radiometric input uncertainties, the estimated output uncertainties for OC and IOP were log-normally distributed (as per Figures 5 and 6). Such highly dynamic and variable nature of uncertainties in ocean color data products highlights the need for these estimates to be done on a pixel-by-pixel basis, rather than single scene-wide estimate, further justifying the need for simplified, computationally inexpensive approach (i.e. FOFM).

We note that our FOFM uncertainty formulation for the GIOP currently does not consider uncertainty in spectral shape models (i.e. $u(a^*_{f,i})$ and $u(b^*_{bp,i})$). Indeed, we believe that this may be why there were some noticeable differences when comparing FOFM and MC methods, for example: when $u(b_{bp,443}) >$ $2.00x10^{-4}$ m^{-1} (Figure 3h). In a cursory study, we re-ran both FOFM and MC calculations with the shape models parametrized as spectral constants (i.e. having no uncertainties). This resulted in improved FOFM-to-MC comparisons (results not shown) and further highlighted how of spectral shape uncertainties impact our FOFM uncertainty estimates. As part of future work, we thus plan to extend our current GIOP FOFM uncertainty formulation to include the spectral shape uncertainties. Additionally, we note that $u(a^*_{f,i})$ and $u(b^*_{bp,i})$, computed as functions of *Chl* and a red-green $R_{rs,i}$ ratio, respectively, are also correlated. Thus, an improved GIOP FOFM uncertainty formulation should also consider covariances between spectral shape models.

3.2.4 GIOP model misfit uncertainties

In this analysis we used our high-quality evaluation R_{rs} dataset to approximate GIOP model misfit uncertainties. Our assumptions in this exercise were: (i) the uncertainties in our R_{rs} dataset are small, and (ii) the least squares residual of the optimal solution (model misfit) are thus due to an imperfect model.

In this analysis we first, computed the error-covariance matrix, $\mathbf{E_{rrs}}$, for each R_{rs} observation as follows: (i) employ the Levenberg-Marquardt non-linear least squares optimization to iteratively find an optimal solution for the free variables x_{ϕ}, x_{dg}, and x_p which correspond to *Chl* concentration, $a_{dg,440}$, and $b_{bp,440}$, respectively (see Appendix E for further detail). We note that in the standard implementation of the GIOP, the cost function (Chi-squared) is unweighted. (ii) feed the optimal set of x_{ϕ}, x_{dg}, and x_p back in the forward reflectance model to compute a best-fit spectral sub-surface remote sensing reflectance, $r_{rs,i}^{\mathrm{mod}}$. (iii) calculate the spectral residual, $\varepsilon_{rrs,i}$, between $r_{rs,i}^{\mathrm{mod}}$ and sensor-observed subsurface remote sensing reflectance. (iv) set the diagonal elements of $\mathbf{E_{rrs}}$ as the square of $\varepsilon_{rrs,i}$.

Next, by substituting $\mathbf{E_{rrs}}$ for $\mathbf{V_{rrs}}$ in Equation E13 the parameter error-covariance matrix, $\mathbf{E}_x$, can be computed as:

$$\mathbf{E_x} = \mathbf{J}^{-1}\mathbf{E_{rrs}}(\mathbf{J}^{\mathrm{T}})^{-1}$$

Where **J** is the Jacobian matrix of the forward model (see Appendix E for derivation). Finally, the estimates of parameter uncertainties due to model misfit were estimated as the square root of the diagonal elements of $\mathbf{E_{rrs}}$. The model-misfit uncertainties are summarized in Table 9 and compared to parameter uncertainties due to Hu spectrally-dependent radiometric uncertainties (as per Table 7).

We found that estimated GIOP model misfit uncertainties were 60-to-90% smaller than those imparted by radiometric uncertainty. Thus, by combining the two during pixel-by-pixel processing, it would be possible to more completely estimate $u_{measurement}(y)$ for IOPs. However, we accept that our FOFM model-data misfit approach is approximate only and does not consider all uncertainties in the GIOP model formulation.

3.3 Comparing product uncertainties due to various radiometric input uncertainties

In order to evaluate the impact of different R_{rs} uncertainty values on derived product uncertainties, using the FOFM method we: (i) propagated spectrally flat, uncorrelated R_{rs} relative uncertainties of 1, 5, and 10% through OC and IOP models, and (ii) propagated spectrally-dependent, uncorrelated $u(R_{rs})$ through OC and IOP models by linearly interpolating/extrapolating tabulated data published by Hu et al. (2013), referred to as "Hu uncertainties" (see Figure 2). Summary results of this analysis are given in Tables 8 and 9. As expected, introducing spectrally flat, uncorrelated R_{rs} uncertainties of lower and higher value than the previously evaluated 5%, resulted in respectively lower and higher uncertainties in data products, while the distribution of uncertainties kept the same shape as for the 5% run (Figure 6). For the product uncertainties derived using the "Hu R_{rs} uncertainties", both the shape of the distribution and median values changed from the 5% run (Figure 6). These results demonstrate the importance of considering spectral dependence in radiometric uncertainties. Notably, considering spectrally flat 5% relative uncertainties in R_{rs} for a data product such as *nflh*, which utilizes red-end bands, may result in significant underestimation of likely data product uncertainties.

Spectrally flat relative uncertainty in R_{rs} (e.g. 5% in the blue-green region) is a commonly used accuracy goal for ocean color missions. However, we know from on-orbit data that sensors such as SeaWiFS and MODIS have largely not achieved their desired accuracy goals over the full spectral range (Hu et al., 2013), particularly at red wavelengths. In lieu of any knowledge of a sensor's radiometric uncertainty characteristics (e.g. during design trade studies), one might decide to utilize desired relative radiometric accuracy goals to approximate ocean color data product uncertainties. However, our results have shown spectrally flat (5%) and spectrally-dependent (Hu) relative R_{rs} uncertainties lead to different estimates of OC and IOP uncertainties. Indeed, for improved uncertainty estimates, we recommend the use of more representative spectrally-dependent $u(R_{rs})/R_{rs}$, if known.

3.4 Application to satellite chlorophyll image

The potential impact that spectrally-correlated uncertainties in R_{rs} have upon ocean color data product uncertainties was evaluated using a scene of the southern Hawaiian Islands captured on 1 December 2000 (Figure 7). We have estimated on a pixel-by-pixel basis the covariance matrix of remote sensing reflectances, $\mathbf{V}_{\mathrm{Rrs}}$, as per the methodology described in Appendix F. Estimates of $u(Chl)$ were then calculated both with- and without the off-diagonal terms in $\mathbf{V}_{\mathrm{Rrs}}$ to demonstrate the impact of incorporating covariance terms (if known) when estimating uncertainties.

The sample SeaWiFS *Chl* image (Figure 7a) shows clearest waters occurred southeast of Island of Hawaii (largest island) with two large eddies to the west. Regions of elevated *Chl* concentration are also visible along the northeast coast of the Island of Hawaii, and also adjacent to coastal waters of four islands (Maui, Lanai, Molokai, and Kahoolawe) to the northwest of Hawaii. Derived Chl_{blend} ranges from 1.83x10^{-3} – 0.498 mg m^{-3} with a median of 0.066 mg m^{-3}. When the off-diagonal terms in $\mathbf{V}_{\mathrm{Rrs}}$ were considered, the estimated values of $u(Chl)$ ranged from 1.30x10^{-3} – 0.075 mg m^{-3} with a scene-wide median of 5.20 x10^{-3} mg m^{-3} (Figure 7b) and the relative uncertainties spanned 0.84 – 38.6 % with a median of 7.89% (Figure 7c). When the off-diagonal terms in $\mathbf{V}_{\mathrm{Rrs}}$ were not considered (i.e. set to zero), estimated values of $u(Chl)$ ranged from 1.30x10^{-3} – 0.109 mg m^{-3} with a scene-wide median of 5.50 x10^{-3} mg m^{-3} (Figure 7d) and relative uncertainties spanning 0.85 – 46.1 % with a median of 8.27% (Figure 7e). Note, these image statistics were computed with standard NASA level-2 quality control flags applied to remove the effect of: land, clouds, sunglint, land, atmospheric correction failure, product failure, and straylight contamination .

These results demonstrate how a FOFM method can be utilized in operational processing code to estimate uncertainties in derived bio-optical data products. The FOFM method was straightforward to implement within l2gen code and did not add any appreciable processing overhead. Whilst our estimation of $\mathbf{V}_{\mathrm{Rrs}}$ is rudimentary (Appendix F), it allowed us to consider the covariance terms in the FOFM derivation of $u(Chl)$. Critically, we demonstrated that the inclusion of off-diagonal covariance terms from $\mathbf{V}_{\mathrm{Rrs}}$ led to lower estimates of both $u(Chl)$ and $u(Chl)/Chl$ when compared to the same calculations performed with off-diagonal elements of $\mathbf{V}_{\mathrm{Rrs}}$ set to zero; a result consistent with findings of Lamquin et al. (2013). Additionally, this example was done with an operational processing code, demonstrating easiness of implementing a FOFM method within day-to-day ocean color processing.

3.5 POC algorithm case study

Recall from Equation 1, we broadly defined measurement uncertainty as having two sources: data uncertainty and model uncertainty. Throughout this paper we have focused heavily on deriving data uncertainties (i.e. propagation of radiometric uncertainty) which is useful if one is trying understand how a specific sensor's noise characteristics may impact derived data product uncertainties. However, this information alone does not provide a complete picture of a measurement uncertainty; model uncertainty also needs to be considered. We thus wish to demonstrate how with knowledge of model uncertainties one can draw more complete conclusions about biogeochemically-relevant data product uncertainties. As such, we present a case study in which we estimate *POC* measurement uncertainty for two different algorithms: (i) Stramski et al. (2008a) and (ii) Rasse et al. (2017).

Our motivation here is to solely demonstrate how one might develop algorithm uncertainty budgets (data and model uncertainty as per Equation 1) using a FOFM framework. Our calculations, however, are limited by: (i) the representativeness of our in situ R_{rs} dataset which does not encompass all optical water-types found in the World's oceans, (ii) our spectral $u(R_{rs})$ values which are estimated from data published by Hu et al. (2013) for a MODIS-like without co-variance terms, and (iii) our knowledge of model uncertainties, such as coefficients uncertainties, which is limited to those reported in literature and/or our best-guess estimates. We hence caution the reader should not use our reported numbers as a basis for algorithm selection.

3.5.1 *POC measurement uncertainty estimates*

In this exercise, we performed rudimentary calculations to estimate measurement uncertainty budgets for two *POC* algorithms: (i) NASA's standard *POC* algorithm (Stramski et al., 2008a) and (ii) the IOP-based model of Rasse et al. (2017). Conveniently for this exercise, both *POC* models have a power law formulation:

$$POC = a_{poc} X^{b_{poc}} \qquad [6]$$

where X in Stramski et al. (2008a) is a blue-to-green reflectance ratio ($R_{rs,443}/R_{rs,555}$, as per Appendix C) and the coefficients a_{poc} and b_{poc} have the values of 203.2 and -1.034, respectively. For the approach of Rasse et al. (2017) X is $b_{bp,547}$ and the coefficients a_{poc} and b_{poc} have the values of 141,253 and 1.18, respectively. Note, in this case study we use GIOP-derived estimates of $b_{bp,547}$ as inputs to the Rasse et al. (2017) model.

First, let us consider the model uncertainty component due to imperfect model coefficients. For both *POC* algorithms, with the coefficients a_{poc} and b_{poc} and their assigned uncertainties of $u_{model}(a_{poc})$ and $u_{model}(b_{poc})$, respectively, we can estimate the model variance for *POC* as:

$$u^2_{\text{model}}(POC) = \left(X^{b_{poc}}\right)^2 u^2_{\text{model}}(a_{poc}) + \left(a_{poc} X^{b_{poc}} \log(X)\right)^2 u^2_{\text{model}}(b_{poc}) + \left(a_{poc} b_{poc} X^{b_{poc}-1}\right)^2 u^2_{\text{model}}(X) \qquad [7]$$

In the third term on the right-hand side of Equation 7, we set $u_{model}(X)$=0 and $u_{model}(X)$=$u_{model}(b_{bp,470})$ for Stramski et al. (2008a) and Rasse et al. (2017), respectively. We have also assumed the covariance of the coefficients a_{poc} and b_{poc}, which are determined by regression fit, is zero. For the Rasse et al. (2017) model, the reported model coefficient uncertainties $u_{model}(a_{poc})$ and $u_{model}(b_{poc})$ are 45,534 and 0.046, respectively. For the Stramski et al. (2008a) model values of $u_{model}(a_{poc})$ and $u_{model}(b_{poc})$ were not reported. We did, however, estimate these model uncertainties by reanalyzing the original published dataset of Stramski et al. (2008b) and considering the likely uncertainty introduced by not accounting for the effect of filter pad absorption of *POC* (Novak et al., 2018). Following this cursory analysis (results not shown), we estimated $u_{model}(a_{poc})$ and $u_{model}(b_{\mathrm{poc}})$ for the Stramski et al. (2008a) model to be approximately 2.20 and 0.015, respectively.

Next, we considered the data uncertainty component. The Stramski et al. (2008a) model's data uncertainty FOFM calculus was formulated in Appendix C. For the Rasse et al. (2017) model, we first estimated $u_{data}(b_{bp,547})$. To do so, $b_{bp,547}$ was calculated from GIOP-derived $b_{bp,440}$ as:

$$b_{bp,470} = b_{bp,440} \times \left(\frac{440}{470}\right)^{g}. \qquad [8]$$

The variance in $b_{bp,470}$ due to data uncertainty was then estimated as:

$$u_{data}^{2}(b_{bp,470}) = \left(\frac{\partial b_{bp,470}}{\partial b_{bp,440}}\right)^{2} u_{data}^{2}(b_{bp,440}) + \left(\frac{\partial b_{bp,470}}{\partial g}\right)^{2} u_{data}^{2}(g) + 2\frac{\partial b_{bp,470}}{\partial b_{bp,440}}\frac{\partial b_{bp,470}}{\partial g} u_{data}^{2}(b_{bp,440}, g) \qquad [9]$$

For this exercise, we used GIOP-derived values of $u_{data}(b_{bp},547)$ and $u(\gamma)$. The correlation between derived values of b_{bp},547 and γ was used to estimate the covariance term $u(b_{bp,547}, \gamma)$ as -1.64x10^{-6} m^{-1} nm^{-1}. Using, the GUM methodology the variance in the Rasse et al. (2017) *POC* model due to data uncertainty was then estimated as:

$$u_{data}^{2}(POC) = \left(a_{poc} b_{poc} (b_{bp,470})^{b_{poc}-1}\right)^{2} u_{data}^{2}(b_{bp,470}) \qquad [10]$$

We finally estimated the measurement uncertainty budgets for both *POC* models using our R_{rs} evaluation dataset and with Hu spectrally-dependent, uncorrelated radiometric uncertainties (results are shown in Table10).

In our rudimentary measurement uncertainty budget for the Stramski et al. (2008a) *POC* algorithm, we found the contribution of data (radiometric) uncertainty was larger than model uncertainty. Conversely, for the Rasse et al. (2017) *POC* algorithm, the contribution of model uncertainty was larger than data uncertainty. Whilst these *POC* algorithm uncertainty budgets may not be fully representative due to the assumptions we partook here, the exercise nonetheless demonstrates an important point: that data and model uncertainties should both be considered if one wishes to use uncertainties as a means of benchmarking/comparing ocean color algorithms.

From an algorithm development perspective one can also use FOFM method to explore the relative contribution of individual uncertainty sources to the combined measurement uncertainty. We have graphically displayed the estimated component uncertainty contribution for each *POC* algorithm using pie charts (Figure 8). Such information may assist algorithm designers identify and minimize uncertainty sources within a model.

3.5.2 Summary of POC case study

Our brief example demonstrates the benefits of using the FOFM method for analytically estimating measurement uncertainty in *POC*. From an ecological perspective, this is particularly useful if one is trying to understand the variability in observed patterns, and distinguish real change from variation in uncertainty. Additionally, it allows for sensitivity analysis, thereby providing a guideline for improving model parameterization. The case study demonstrates how an uncertainty budget can provide additional information to end-users regarding data product quality, potentially informing algorithm selection, and/or guiding new algorithm development. Although ocean color algorithms are typically benchmarked based upon validation matchup metrics (Seegers et al., 2018), we expect model selection and development may be better guided by considering how data and model uncertainties manifest in derived data products.

This case study highlights a challenge if one wishes to compare/benchmark legacy ocean color algorithms based on their measurement uncertainty; one must have reasonable and complete knowledge of both data and model uncertainties to do so. Whilst we have demonstrated that it is possible to estimate and propagate random radiometric uncertainties using the FOFM framework, estimating model uncertainties remains a challenge. This is because model component uncertainties (e.g. model coefficient uncertainties) of legacy ocean color algorithms were not routinely reported. To address this, re-analysis of the structure of legacy ocean color algorithms using high quality bio-optical datasets, such as NASA's bio-Optical Marine Algorithm Dataset (Werdell & Bailey, 2005), may be necessary. Without such knowledge, it remains a challenge to formulate complete measurement uncertainty budgets for legacy ocean color algorithms.

4 Conclusions

In this paper we demonstrated a FOFM-based method for estimating uncertainties in a selection of NASA OC and IOP products, namely: *Chl*, $K_{d,490}$, *POC*, *nflh*, $a_{nw,440}$, $a_{\phi,440}$, $a_{dg,440}$, and $b_{bp,440}$, due to sensor-observed radiometric uncertainty. Using a high quality hyperspectral R_{rs} dataset, subsampled to our target wavelengths, we first appraised the FOFM methodology by comparing FOFM-derived uncertainty estimates with uncertainties estimated from MC simulations with an assumed relative spectrally flat, uncorrelated uncertainty in R_{rs} of 5%. Our analyses showed that OC and IOP uncertainties estimated using the FOFM method generally agreed with MC simulations. Collectively, the FOFM-to-MC comparisons provided a basis for checking the correctness of the FOFM formulations, that are often algebraically complex. Further, we demonstrated that the FOFM formulation, which is computationally inexpensive, can be applied in routine pixel-by-pixel data processing for estimating uncertainties in derived ocean color data products.

This manuscript has primarily focused on propagating radiometric uncertainties through bio-optical models ($u_{data}(y)$ in Equation 1). In practice, the combined measurement uncertainty in derived ocean color data products is expected to be larger once model uncertainties are included. In this study, we have broadly assumed that coefficients within the bio-optical algorithms themselves are errorless, which is not the case. Indeed, most coefficients in bio-optical algorithms that have been derived empirically using *in situ* oceanographic datasets, which themselves have inherent uncertainties due to measurement method and environmental variability. The GIOP, for example, makes assumptions about spectral shapes of IOPs, utilizes an approximate forward reflectance model (Gordon et al., 1988), and employs a model to convert $R_{rs,i}$ to $r_{rs,i}$ (Lee et al., 2002). Thus, there are a number of GIOP model components whose uncertainties, if characterized, may improve the overall estimate of IOP measurement uncertainty. Our case study of *POC* algorithms also highlighted how the addition of model (e.g. coefficient) uncertainties can further inform end-users, and may potentially guide algorithm development and/or selection.

Although this work represents a first step towards implementing pixel-by-pixel uncertainty estimates in NASA operational ocean color processing code, we recognize that continued effort is required. For example, strategies for quantifying uncertainties in look-up-table (LUT) based models, such as the two-band particulate inorganic carbon (PIC) algorithm (Balch et al., 2005) and bidirectional reflectance distribution function (BRDF) correction (Morel et al., 2002), are needed. Globally, there are a multitude of ocean color algorithms maintained by various researchers and/or institutes and formulating uncertainty estimates must be a collective effort. While the community continues to innovate new bio-optical algorithms, we strongly encourage model developers to characterize uncertainties as a matter of routine.

As we enter the hyperspectral world of PACE, it is credible to expect an evolutionary leap in remote sensing observation of ocean processes; detailing the phytoplankton diversity, its physiological preferences, and ecology from space. This, parallel to the increase in computational power of the day-to-day data processing, will allow for more complex algorithms; algorithms which will need detailed evaluation of uncertainty budgets, to understand what is real, and what is hidden under the dashed line.

5 Acknowledgments

Many thanks to NASA Ocean Biology Processing Group staff for their advice during the preparation of this manuscript. The authors are thankful for all the scientists that contributed to collection of this dataset, especially Wayne Slade and Nicole Poulton, and captains and crews of the UNOLS research vessels. We are also very grateful to the two reviewers for their detailed and insightful comments.

6 Author contributions

Conceptualization, methodology, simulations, and data analysis: LM, IC, and JW; Hyperspectral dataset: AC and IC; Original draft, reviewing, and editing: LM, IC, JW and AC.

7 Funding

This research was funded by the National Aeronautics and Space Administration (NASA) Ocean Biology and Biogeochemistry Program via an award under the solicitation *The Science of Terra, Aqua, and Suomi NPP*, Ocean Biology and Biogeochemistry (NNX13AC42G), and PACE mission.

8 Conflicts of interest

Author Lachlan McKinna was employed by company Go2Q Pty Ltd. All other authors declare no competing interests.

9 Data Availability Statement

The datasets analyzed in this study can be found in the NASA's SeaBASS, https://seabass.gsfc.nasa.gov/experiment/RemSensPOC and https://seabass.gsfc.nasa.gov/experiment/sabor.

References

Angal, A., Xiong, X. J., Sun, J., & Geng, X. (2015). *On-orbit noise characterization of MODIS reflective solar bands* (Vol. 9): SPIE.

Antoine, D., d'Ortenzio, F., Hooker, S. B., Bécu, G., Gentili, B., Tailliez, D., & Scott, A. J. (2008). Assessment of uncertainty in the ocean reflectance determined by three satellite ocean color sensors (MERIS, SeaWiFS and MODIS-A) at an offshore site in the Mediterranean Sea (BOUSSOLE project). *Journal of Geophysical Research: Oceans, 113*(C7). doi:10.1029/2007JC004472

Bailey, S. W., Franz, B. A., & Werdell, P. J. (2010). Estimation of near-infrared water-leaving reflectance for satellite ocean color data processing. *Optics Express, 18*(7), 7521-7527. doi:10.1364/OE.18.007521

Bailey, S. W., & Werdell, P. J. (2006). A multi-sensor approach for the on-orbit validation of ocean color satellite data products. *Remote Sensing of Environment, 102*(1), 12-23. doi:https://doi.org/10.1016/j.rse.2006.01.015

Balch, W. M., Gordon, H. R., Bowler, B. C., Drapeau, D. T., & Booth, E. S. (2005). Calcium carbonate measurements in the surface global ocean based on Moderate-Resolution Imaging Spectroradiometer data. *Journal of Geophysical Research: Oceans, 110*(C7). doi:10.1029/2004JC002560

Behrenfeld, M. J., Westberry, T. K., Boss, E. S., O'Malley, R. T., Siegel, D. A., Wiggert, J. D., . . . Mahowald, N. (2009). Satellite-detected fluorescence reveals global physiology of ocean phytoplankton. *Biogeosciences, 6*(5), 779-794. doi:10.5194/bg-6-779-2009

Bricaud, A., Morel, A., Babin, M., Allali, K., & Claustre, H. (1998). Variations of light absorption by suspended particles with the chlorophyll a concentration in oceanic (Case 1) waters : analysis and implications for bio-optical models. *J. Geophys. Res. Oceans, 103*, 31,033 - 031,044.

Campbell, J. W. (1995). The lognormal distribution as a model for bio-optical variability in the sea. *Journal of Geophysical Research: Oceans, 100*(C7), 13237-13254. doi:10.1029/95JC00458

Chase, A. P., Boss, E., Cetinić, I., & Slade, W. (2017). Estimation of Phytoplankton Accessory Pigments From Hyperspectral Reflectance Spectra: Toward a Global Algorithm. *Journal of Geophysical Research: Oceans, 122*(12), 9725-9743. doi:10.1002/2017JC012859

Eplee, J. R. E., Patt, F. S., Barnes, R. A., & McClain, C. R. (2007). SeaWiFS long-term solar diffuser reflectance and sensor noise analyses. *Applied Optics, 46*(5), 762-773. doi:10.1364/AO.46.000762

Franz, B. A., Behrenfeld, M. J., Siegel, D. A., & Signorini, S. R. (2017). Global ocean phytoplankton [in: State of the Climate in 2016]. *Bull. Amer. Meteor. Soc, 99*(8), S94-S96. doi:http://doi.org/10.1175/2017BAMSStateoftheClimate.1.

Franz, B. A., & Werdell, P. J. (2010). A Generalized Framework for Modeling of Inherent Optical Propertiesin Ocean Remote Sensing Applications. *Proc. Ocean Optics XX, Anchorage, Alaska, USA, 27 September - 1 October*.

Gillis, D. B., Bowles, J. H., Montes, M. J., & Moses, W. J. (2018). Propagation of sensor noise in oceanic hyperspectral remote sensing. *Optics Express, 26*(18), A818-A831. doi:10.1364/OE.26.00A818

Gordon, H. R., Brown, O. B., Evans, R. H., Brown, J. W., Smith, R. C., Baker, K. S., & Clark, D. K. (1988). A semianalytic radiance model of ocean color. *J. Geophys. Res. Atmos., 93*(D9), 10909-10924. doi:10.1029/JD093iD09p10909

Gordon, H. R., & Wang, M. (1994). Retrieval of water-leaving radiance and aerosol optical thickness over the oceans with SeaWiFS: a preliminary algorithm. *Applied Optics, 33*(3), 443-452. doi:10.1364/AO.33.000443

Gould, W. G., McCarthy, S. E., Coelho, E., Shulman, I., & Richman, J. G. (2014). Combining satellite ocean color and hydrodynamic model uncertainties in bio-optical forecasts. *Journal of Applied Remote Sensing, 8*(1), 083652 doi:10.117/1.JRS.8.083652

Hooker, S. B., Esaias, W. E., Feldman, G. C., Gregg, W. W., & McClain, C. R. (1992). *An Overview of SeaWiFS and Ocean Color*. Retrieved from Greenbelt:

Hooker, S. B., & McClain, C. R. (2000). The calibration and validation of SeaWiFS data. *Progress in Oceanography, 45*(3), 427-465. doi:https://doi.org/10.1016/S0079-6611(00)00012-4

Hu, C., Feng, L., & Lee, Z. (2013). Uncertainties of SeaWiFS and MODIS remote sensing reflectance: Implications from clear water measurements. *Remote Sensing of Environment, 133*, 168-182. doi:https://doi.org/10.1016/j.rse.2013.02.012

Hu, C., Feng, L., Lee, Z., Davis, C. O., Mannino, A., McClain, C. R., & Franz, B. A. (2012). Dynamic range and sensitivity requirements of satellite ocean color sensors: learning from the past. *Applied Optics, 51*(25), 6045-6062. doi:10.1364/AO.51.006045

Hu, C., Lee, Z., & Franz, B. (2012). Chlorophyll a algorithms for oligotrophic oceans: A novel approach based on three-band reflectance difference. *Journal of Geophysical Research: Oceans, 117*(C1), n/a-n/a. doi:10.1029/2011JC007395

IOCCG. (2008). *Why Ocean Colour? The Societal Benefits of Ocean- Colour Technology* (Vol. 7). Dartmouth, Canada: IOCCG.

Jay, S., Guillaume, M., Chami, M., Minghelli, A., Deville, Y., Lafrance, B., & Serfaty, V. (2018). Predicting minimum uncertainties in the inversion of ocean color geophysical parameters based on Cramer-Rao bounds. *Optics Express, 26*(2), A1-A18. doi:10.1364/OE.26.0000A1

JCGM. (2008). *Evaluation of measurement data - Guide to the expression of uncertainty in measurement*. Retrieved from JCGM 100:2008:

Lamquin, N., Mangin, A., Mazeran, C., Bourg, B., Bruniquel, V., & D'Andon, O. F. (2013). *OLCI L2 pixel-by-pixel uncertainty propagation in OLCI clean water branch*: ESA ATBD ref. S3-L2-SD-01-C01-ACR-TN.

Lee, Z., Arnone, R., Hu, C., Werdell, P. J., & Lubac, B. (2010). Uncertainties of optical parameters and their propagations in an analytical ocean color inversion algorithm. *Applied Optics, 49*(3), 369-381. doi:10.1364/AO.49.000369

Lee, Z., Carder, K. L., & Arnone, R. A. (2002). Deriving inherent optical properties from water color: a multiband quasi-analytical algorithm for optically deep waters. *Applied Optics, 41*(27), 5755-5772. doi:10.1364/AO.41.005755

Maritorena, S., d'Andon, O. H. F., Mangin, A., & Siegel, D. A. (2010). Merged satellite ocean color data products using a bio-optical model: Characteristics, benefits and issues. *Remote Sensing of Environment, 114*(8), 1791-1804. doi:https://doi.org/10.1016/j.rse.2010.04.002

McClain, C. R. (2009). A Decade of Satellite Ocean Color Observations. *Annual Review of Marine Science, 1*(1), 19-42. doi:10.1146/annurev.marine.010908.163650

McClain, C. R., Feldman, G. C., & Hooker, S. B. (2004). An overview of the SeaWiFS project and strategies for producing a climate research quality global ocean bio-optical time series. *Deep Sea Research Part II: Topical Studies in Oceanography, 51*(1), 5-42. doi:https://doi.org/10.1016/j.dsr2.2003.11.001

McKinna, L. I. W., Werdell, P. J., & Proctor, C. W. (2016). Implementation of an analytical Raman scattering correction for satellite ocean-color processing. *Optics Express, 24*(14), A1123-A1137. doi:10.1364/OE.24.0A1123

Mekid, S., & Vaja, D. (2008). Propagation of uncertainty: Expressions of second and third order uncertainty with third and fourth moments. *Measurement, 41*(6), 600-609. doi:https://doi.org/10.1016/j.measurement.2007.07.004

Melin, F. (2010). Global Distribution of the Random Uncertainty Associated With Satellite-Derived Chl <emphasis emphasistype="italic">a</emphasis>. *IEEE Geoscience and Remote Sensing Letters, 7*(1), 220-224. doi:10.1109/LGRS.2009.2031825

Mélin, F., Sclep, G., Jackson, T., & Sathyendranath, S. (2016). Uncertainty estimates of remote sensing reflectance derived from comparison of ocean color satellite data sets. *Remote Sensing of Environment, 177*, 107-124. doi:https://doi.org/10.1016/j.rse.2016.02.014

Moore, T. S., Campbell, J. W., & Dowell, M. D. (2009). A class-based approach to characterizing and mapping the uncertainty of the MODIS ocean chlorophyll product. *Remote Sensing of Environment, 113*(11), 2424-2430. doi:https://doi.org/10.1016/j.rse.2009.07.016

Morel, A., Antoine, D., & Gentili, B. (2002). Bidirectional reflectance of oceanic waters: accounting for Raman emission and varying particle scattering phase function. *Applied Optics, 41*(30), 6289-6306. doi:10.1364/AO.41.006289

Mueller, J. L. (2000). SeaWiFS algorithm for the diffuse attenuation coefficient, K(490), using water-leaving radiances at 490 and 555 nm. In S. B. Hooker & E. Firestone, R (Eds.), *NASA Technical Memorandum 2000-206829* (Vol. 11, pp. 51). Greenbelt, USA: NASA Goddard Space Flight Center.

Neukermans, G., Ruddick, K., Bernard, E., Ramon, D., Nechad, B., & Deschamps, P.-Y. (2009). Mapping total suspended matter from geostationary satellites: a feasibility study with SEVIRI in the Southern North Sea. *Optics Express, 17*(16), 14029-14052. doi:10.1364/OE.17.014029

Novak, M. G., Cetinić, I., Chaves, J. E., & Mannino, A. (2018). The adsorption of dissolved organic carbon onto glass fiber filters and its effect on the measurement of particulate organic carbon: A laboratory and modeling exercise. *Limnology and Oceanography: Methods, 16*(6), 356-366. doi:10.1002/lom3.10248

O'Reilly, J. E., Maritorena, S., Mitchell, B. G., Siegel, D. A., Carder, K. L., Garver, S. A., . . . McClain, C. (1998). Ocean color chlorophyll algorithms for SeaWiFS. *J. Geophys. Res. Oceans, 103*(C11), 24937-24953. doi:10.1029/98JC02160

PACE Science Definition Team. (2018). *Pre-Aerosol, Clouds, and ocean Ecosystem (PACE) Mission Science Definition Team Report*. Retrieved from Greenbelt, MD:

Putko, M. M., Taylor, I. I. I. A. C., Newman, P. A., & Green, L. L. (2001). Approach for Input Uncertainty Propagation and Robust Design in CFD Using Sensitivity Derivatives. *Journal of Fluids Engineering, 124*(1), 60-69. doi:10.1115/1.1446068

Qi, L., Lee, Z., Hu, C., & Wang, M. (2017). Requirement of minimal signal-to-noise ratios of ocean color sensors and uncertainties of ocean color products. *Journal of Geophysical Research: Oceans, 122*(3), 2595-2611. doi:10.1002/2016JC012558

Rasse, R., Dall'Olmo, G., Graff, J., Westberry, T. K., van Dongen-Vogels, V., & Behrenfeld, M. J. (2017). Evaluating Optical Proxies of Particulate Organic Carbon across the Surface Atlantic Ocean. *Frontiers in Marine Science, 4*(367). doi:10.3389/fmars.2017.00367

Refsgaard, J. C., van der Sluijs, J. P., Højberg, A. L., & Vanrolleghem, P. A. (2007). Uncertainty in the environmental modelling process – A framework and guidance. *Environmental Modelling & Software, 22*(11), 1543-1556. doi:https://doi.org/10.1016/j.envsoft.2007.02.004

Salama, M. S., Dekker, A., Su, Z., Mannaerts, C. M., & Verhoef, W. (2009). Deriving inherent optical properties and associated inversion-uncertainties in the Dutch Lakes. *Hydrol. Earth Syst. Sci.*, *13*(7), 1113-1121. doi:10.5194/hess-13-1113-2009

Salama, M. S., Mélin, F., & Van der Velde, R. (2011). Ensemble uncertainty of inherent optical properties. *Optics Express, 19*(18), 16772-16783. doi:10.1364/OE.19.016772

Seegers, B. N., Stumpf, R. P., Schaeffer, B. A., Loftin, K. A., & Werdell, P. J. (2018). Performance metrics for the assessment of satellite data products: an ocean color case study. *Optics Express*, *26*(6), 7404-7422. doi:10.1364/OE.26.007404

Stramski, D., Reynolds, R. A., Babin, M., Kaczmarek, S., Lewis, M. R., Rˆttgers, R. d., . . . Claustre, H. (2008b) Concentration of particulate organic carbon and optical properties in the eastern South Pacific and eastern Atlantic Oceans. *Supplement to: Stramski, D et al. (2008): Relationships between the surface concentration of particulate organic carbon and optical properties in the eastern South Pacific and eastern Atlantic Oceans. Biogeosciences, 5, 171-201, https://doi.org/10.5194/bg-5-171-2008*: PANGAEA.

Stramski, D., Reynolds, R. A., Babin, M., Kaczmarek, S., Lewis, M. R., Rottgers, R., . . . Claustre, H. (2008a). Relationships between the surface concentration of particulate organic carbon and optical properties in the eastern South Pacific and eastern Atlantic Oceans. *Biogeosciences, 5*(1), 171-201. doi:10.5194/bg-5-171-2008

Thuillier, G., Hersé, M., Labs, D., Foujols, T., Peetermans, W., Gillotay, D., . . . Mandel, H. (2003). The Solar Spectral Irradiance from 200 to 2400 nm as Measured by the SOLSPEC Spectrometer from the Atlas and Eureca Missions. *Solar Physics*, *214*(1), 1-22. doi:10.1023/A:1024048429145

Wang, P., Boss, E. S., & Roesler, C. (2005). Uncertainties of inherent optical properties obtained from semianalytical inversions of ocean color. *Applied Optics, 44*(19), 4074-4085. doi:10.1364/AO.44.004074

Werdell, P. J., & Bailey, S. W. (2005). An improved in-situ bio-optical data set for ocean color algorithm development and satellite data product validation. *Remote Sensing of Environment, 98*(1), 122-140. doi:http://dx.doi.org/10.1016/j.rse.2005.07.001

Werdell, P. J., Franz, B. A., Bailey, S. W., Feldman, G. C., Boss, E., Brando, V. E., . . . Lee, Z. (2013). Generalized ocean color inversion model for retrieving marine inherent optical properties. *Applied Optics, 52*(10), 2019-2037.

Westberry, T. K., Boss, E., & Lee, Z. (2013). Influence of Raman scattering on ocean color inversion models. *Applied Optics*, *52*(22), 5552-5561. doi:10.1364/AO.52.005552

10 Tables

Table 1. Bio-optical ocean color data products

Product name	Product suite	Symbol	Units	Reference
Chlorophyll-a pigment concentration*	OC	Chl	mg m^{-3}	Hu, Lee, et al. (2012); O'Reilly et al. (1998)
Chlorophyll-a derived from band ratio	-	Chl_{BR}	mg m^{-3}	O'Reilly et al. (1998)
Chlorophyll-a derived from line height	-	Chl_{LH}	mg m^{-3}	Hu, Lee, et al. (2012)
Diffuse attenuation coefficient at 490 nm	OC	$K_{d,490}$	m^{-1}	Mueller (2000)
Particulate organic carbon	OC	POC	mg m^{-3}	Stramski et al. (2008a)
Normalized fluorescent line height	OC	nflh	mW cm^{-2} µm^{-1} sr^{-1}	Behrenfeld et al. (2009)
Absorption coefficient of total non-water components 443 nm	IOP	$a_{nw,443}$	m^{-1}	Werdell et al. (2013)
Absorption coefficient of phytoplankton at 443 nm	IOP	$a_{\phi,443}$	m^{-1}	Werdell et al. (2013)
Absorption coefficient of colored dissolved and detrital matter at 443 nm	IOP	$a_{dg,443}$	m^{-1}	Werdell et al. (2013)
Particulate backscattering coefficient at 443 nm	IOP	$b_{bp,44}$	m^{-1}	Werdell et al. (2013)

*Note that NASA's standard *Chl* product is a dynamic blend of Chl_{BR} and Chl_{LH}

Table 2. Log-normal statistics comparing Monte Carlo (MC) and first-order first-moment (FOFM) uncertainty calculations for Rrs with spectrally flat, uncorrelated 5% relative uncertainty

	Derived product uncertainty	
Product	Bias	Slope
Chl (all)	0.95	0.96
Chl_{BR}	1.00	1.00
Chl_{LH}	0.99	1.00
$Chl_{blended}^{*}$	0.73	0.72
$K_{d,490}$	0.99	1.00
POC	0.99	1.00
$nflh$	0.99	1.00
$a_{nw,443}$	0.99	1.00
$a_{\phi,443}$	0.98	1.00
$a_{dg,443}$	0.98	1.00
$b_{bp,443}$	0.99	0.98

*Blended LH and BR *Chl* product span 0.134 – 0.165 mg m^{-3}.

Table 3. OC products and associated uncertainties derived via MC method with 5%, uncorrelated relative uncertainty in R_{rs}

	Derived value		Absolute uncertainty		Relative uncertainty (%)	
Product	Range	Median	Range	Median	Range	Median
Chl (mg m^{-3})	3.96x10^{-2} – 1.27	0.110	2.56x10^{-5} – 0.231	7.00x10^{-3}	1.73– 18.2	9.74
$K_{d,490}$ (m^{-1})	2.01x10^{-2} - 0.131	2.91 x10^{-2}	1.19x10^{-3} – 1.36x10^{-2}	2.68x10^{-3}	5.92 – 10.5	8.94
POC (mg m^{-3})	18.8 – 203.4	33.1	1.37 – 14.6	2.44	7.11 -7.60	7.37
nflh (mW cm^{-2} µm^{-1} sr^{-1})	5.25 x10^{-6} – 2.74 x10^{-2}	2.20 x10^{-3}	3.18 x10^{-4} – 4.47 x10^{-3}	9.86x10^{-4}	14.8 – 1.7 x10^{4}	41.9

Table 4. OC products and associated uncertainties derived via FOFM method with 5%, uncorrelated relative uncertainty in R_{rs}

	Derived value		Absolute uncertainty		Relative uncertainty (%)	
Product	Range	Median	Range	Median	Range	Median
Chl (mg m^{-3})	3.96 x10^{-2} – 1.28	0.110	3.89x10^{-5} – 0.230	6.70 x10^{-3}	0.26 – 18.7	9.67
$K_{d,490}$ (m^{-1})	2.01x10^{-2} - 0.131	2.91x10^{-2}	1.18x10^{-3} – 1.33x10^{-2}	2.68x10^{-3}	5.86 – 10.2	8.91
POC (mg m^{-3})	18.8 – 203.4	33.1	1.37 – 14.9	2.42	7.31*	7.31
nflh (mW cm^{-2} µm^{-1} sr^{-1})	2.05x10^{-6} – 2.73x10^{-2}	2.19Ex10^{-3}	3.21x10^{-4} – 4.43x10^{-3}	9.87x10^{-4}	15.1 – 3.24 x10^{4}	42.1

*Relative uncertainties in POC computed using FOFM method were constant over the dynamic range

Table 5. IOP products and associated uncertainties derived using MC method with 5%, uncorrelated relative uncertainty in R_{rs}

	Derived value		Absolute uncertainty		Relative uncertainty (%)	
Product	Range	Median	Range	Median	Range	Median
a_{nw}(443) (m^{-1})	9.40x10^{-3} – 0.127	0.0185	1.79 x10^{-3} – 1.13x10^{-2}	2.31x10^{-3}	8.16 – 19.4	12.6
a_{ϕ}(443) (m^{-1})	5.80x10^{-3} – 9.43 x10^{-2}	9.60x10^{-3}	1.63x10^{-3} – 9.68x10^{-3}	2.04x10^{-3}	10.0 – 29.2	21.4
a_{dg}(443) (m^{-1})	3.50x10^{-3} – 3.72 x10^{-2}	8.71x10^{-3}	6.66x10^{-4} – 5.90x10^{-3}	1.07x10^{-3}	7.92 – 19.9	14.5
b_{bp}(443) (m^{-1})	4.18x10^{-4} – 4.00 x10^{-3}	1.08x10^{-3}	8.98x10^{-5} – 2.25Ex10^{-4}	1.34x10^{-4}	5.57 – 34.1	13.8

Table 6. IOP products and associated uncertainties derived using FOFM method with 5%, uncorrelated relative uncertainty in R_{rs}

	Derived value		Absolute uncertainty		Relative uncertainty (%)	
Product	Range	Median	Range	Median	Range	Median
$a_{tw,443}$ (m^{-1})	$9.42\text{x}10^{-3}$ – 0.127	0.0185	$1.79\text{x}10^{-3}$ – $1.03\text{x}10^{-2}$	$2.26\text{x}10^{-3}$	8.12 – 19.1	12.2
$a_{\phi,443}$ (m^{-1})	$5.86\text{x}10^{-3}$ – $9.45\text{x}10^{-2}$	9.63E-3	$1.64\text{x}10^{-4}$ – $8.73\text{x}10^{-3}$	$2.00\text{x}10^{-3}$	9.02 – 28.6	20.8
$a_{dg,443}$ (m^{-1})	$3.51\text{x}10^{-3}$ – $3.70\text{x}10^{-2}$	8.73E-3	$6.51\text{x}10^{-4}$ – $5.63\text{x}10^{-3}$	$1.05\text{x}10^{-3}$	7.93 – 18.9	14.1
$b_{bp,443}$ (m^{-1})	$4.16\text{x}10^{-4}$ – $4.01\text{x}10^{-3}$	1.00E-3	$9.00\text{x}10^{-5}$ – $2.11\text{x}10^{-4}$	$1.33\text{x}10^{-4}$	5.25 – 34.1	13.9

Table 7: GIOP model-misfit uncertainties estimated using the evaluation *R_{rs}* dataset.

	Absolute uncertainty (m^{-1})		Relative uncertainty (%)		Difference between absolute data and absolute model misit uncertainties* (%)
Product	Range	Median	Range	Median	Median
$a_{tw,443}$ (m^{-1})	$3.88\text{x}10^{-4}$ – $5.71\text{x}10^{-3}$	$4.87\text{x}10^{-4}$	1.26 – 5.70	3.15	-77
$a_{\phi,443}$ (m^{-1})	$3.67\text{x}10^{-4}$ – $5.25\text{x}10^{-3}$	$4.54\text{x}10^{-4}$	3.02 – 9.09	4.68	-77
$a_{dg,443}$ (m^{-1})	$1.07\text{x}10^{-4}$ – $2.26\text{x}10^{-3}$	$1.434\text{x}10^{-4}$	0.81 – 7.48	2.86	-86
$b_{bp,443}$ (m^{-1})	$2.94\text{x}10^{-5}$ – $2.17\text{x}10^{-4}$	$5.22\text{x}10^{-5}$	1.57 – 9.58	4.52	-61

*Difference between median absolute model uncertainties in Table 9 relative to radiometric uncertainties (column RU: Hu in in Table 8) .

Table 8: Median OC data product uncertainties computed as relative uncertainties (RU) in *Rrs* vary.

	Median absolute uncertainties				Median relative uncertainties (%)			
	RU: 1%	**RU: 5%**	**RU: 10%**	**RU: Hu**	**RU: 1%**	**RU: 5%**	**RU: 10%**	**RU: Hu**
Product								
Chl (mg m^{-3})	$1.52\text{x}10^{-3}$	$6.70\text{x}10^{-3}$	$1.46\text{x}10^{-2}$	$6.50\text{x}10^{-3}$	1.96	9.67	19.35	8.29
$K_{d,490}$ (m^{-1})	$5.37\text{x}10^{-4}$	$2.68\text{x}10^{-3}$	$5.36\text{x}10^{-3}$	$5.07\text{x}10^{-3}$	1.78	8.91	17.8	17.3
POC (mg m^{-3})	$4.84\text{x}10^{-1}$	2.42	4.84	4.38	1.46	7.31	14.6	13.1
nflh (mW cm^{-2} µm^{-1} sr^{-1})	$1.97\text{x}10^{-4}$	$9.87\text{x}10^{-4}$	$1.97\text{x}10^{-3}$	$4.47\text{x}10^{-3}$	8.41	42.1	84.1	197.6

Table 9: Median IOP data product uncertainties computed as relative uncertainties (RU) in *Rrs* vary.

	Median absolute uncertainties				Median relative uncertainties (%)			
	RU: 1%	**RU: 5%**	**RU: 10%**	**RU: Hu**	**RU: 1%**	**RU: 5%**	**RU: 10%**	**RU: Hu**
Product								
$a_{tw,443}$ (m^{-1})	4.52x10^{-4}	2.26x10^{-3}	4.52x10^{-3}	2.76x10^{-3}	2.45	12.2	24.5	15.1
$a_{\phi,443}$ (m^{-1})	4.00x10^{-4}	2.00x10^{-3}	4.00x10^{-3}	2.42x10^{-3}	4.15	20.8	41.6	23.8
$a_{dg,443}$ (m^{-1})	2.11x10^{-4}	1.05x10^{-3}	2.11x10^{-3}	1.33x10^{-3}	2.82	14.1	28.2	15.9
$b_{bp,443}$ (m^{-1})	2.67x10^{-5}	1.33x10^{-4}	2.67x10^{-4}	1.73x10^{-4}	2.78	13.9	27.9	17.9

Table 10: Simplified random uncertainty budgets for two *POC* models. Median absolute uncertainties and median relative uncertainties were computed using our R_{rs} evaluation dataset with Hu spectrally-dependent, uncorrelated radiometric uncertainties and basic knowledge of model coefficient uncertainty. We note that these data are intended to illustrate how one might formulate measurement uncertainty budgets. These data are not intended for algorithm comparison purposes.

Algorithm	**Median derived value (mg m^{-3})**	**Median absolute uncertainty in mg m^{-3} (median relative uncertainty in %)**		
		data	*model*	*measurement*
Stramski et al. (2008a)	33.1	4.40 (13.1)	0.94 (2.85)	4.50 (16.6)
Rasse et al. (2017)	37.8	6.96 (18.4)	17.30 (45.8)	18.6 (49.2)

11 Figure captions

Figure 1: Hyperspectral remote-sensing reflectances (n=1124) used in this study.

Figure 2: Relative uncertainties of R_{rs} varying with Chl concentration. Original data taken from Hu et al. (2013) and interpolated to the multispectral resolution used in this study.

Figure 3: Scatter plot comparisons of data product uncertainties estimated (FOFM) with those estimated from Monte Carlo (MC) simulations. (A-D) OC products Chl, $K_{d,490}$, POC, and nflh, respectively. Note that the scatter plot of Chl uncertainty is color coded with respect to the method use to derive the output product (line height: purple, band ratio: green, blended: yellow). (E-H) IOP products $a_{nw,443}$, $a_{\phi,443}$, $a_{dg,443}$, and $b_{bp,443}$, respectively.

Figure 4: (A-D) histograms of derived *Chl*, $K_d(490)$, *POC*, and nflh, respectively. (E-H) histograms of FOFM-estimated uncertainties in derived *Chl*, $K_d(490)$, *POC*, and nflh, respectively. (I-L) histograms of FOFM-estimated relative uncertainties in derived *Chl*, $K_d(490)$, *POC*, and *nflh*, respectively computed using 5% spectrally flat, uncorrelated uncertainty in input R_{rs}. Note: FOFM-estimates of POC relative uncertainties in this study were constant. Dashed curves represent MC results, solid blue bars represent FOFM results

Figure 5: (A-D) histograms of derived $a_{nw,443}$, $a_{dg,443}$, $a_{\phi,443}$, and $b_{bp,443}$, respectively. (E-H) histograms of FOFM-estimated uncertainties in derived $a_{nw,443}$, $a_{dg,443}$, $a_{\phi,443}$, and $b_{bp,443}$, respectively. (I-L) histograms of FOFM-estimated relative uncertainties in derived $a_{nw.443}$, $a_{dg,443}$, $a_{\phi,443}$, and $b_{bp,443}$, respectively computed using 5% spectrally flat, uncorrelated uncertainty in input R_{rs}. Dashed curves represent MC results, solid blue bars represent FOFM results.

Figure 6: Upper row are histograms of derived OC data products uncertainties estimated using the FOFM method. Bottom row are histograms of derived IOP data product uncertainties estimated using the FOFM method. The four histograms in each subplot correspond to four different input $u(R_{rs})$: spectrally flat R_{rs} relative uncertainties of 1% (dashed black), 5% (blue) and 10% (orange) as well as spectrally dependent relative uncertainties taken from (Hu et al., 2013) outlined in green dashed line.

Figure 7: Derived data products for a SeaWiFS image of waters surrounding the Hawaii Islands captured on 1 December 2000. (a) Chl concentration derived using OCI algorithm, (b) u(Chl) computed with covariances included, (c) relative uncertainty in Chl computed with estimated R_{rs} covariances included, (d) u(Chl) calculated without estimated R_{rs} covariances included, and (e) relative uncertainty in Chl computed estimated R_{rs} covariances included.

Figure 8: Pie charts here demonstrate how individual uncertainty sources contribute to estimates of measurement uncertainty. Here we consider: (A) a blue-green band-ratio POC algorithm and (B) an IOP-based POC algorithm. We note that these examples are intended to illustrate how one might visualize source contributions measurement uncertainty. These plots are not intended for algorithm comparison purposes.

12 Figures

Figure 1: Hyperspectral remote-sensing reflectances (N=1124) used in this study.

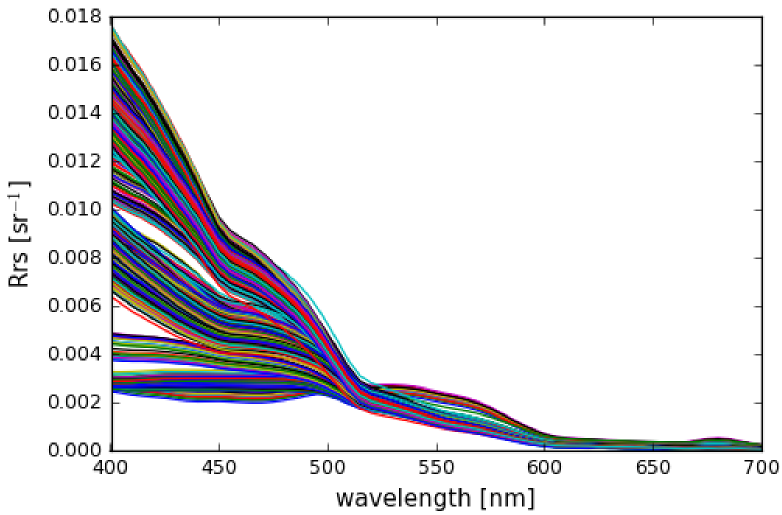

Figure 2: Relative uncertainties of R_{rs} varying with Chl concentration. Original data taken from Hu et al. (2013) and interpolated to the multispectral resolution used in this study.

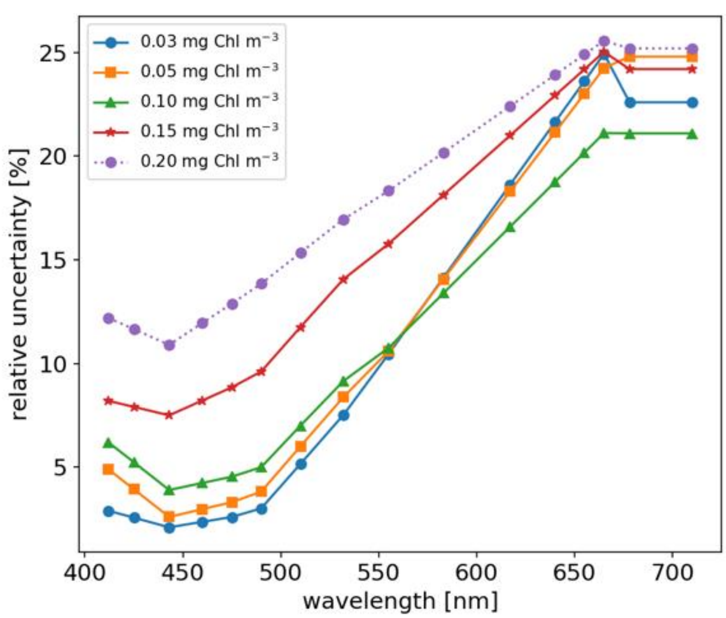

Figure 3: Scatter plot comparisons of data product uncertainties estimated (FOFM) with those estimated from Monte Carlo (MC) simulations. (A-D) OC products Chl, $K_{d,490}$, POC, and nflh, respectively. Note that the scatter plot of Chl uncertainty is color coded with respect to the method use to derive the output product (line height: purple, band ratio: green, blended: yellow). (E-H) IOP products $a_{nw,443}$, $a_{\phi,443}$, $a_{dg,443}$, and $b_{bp,443}$, respectively.

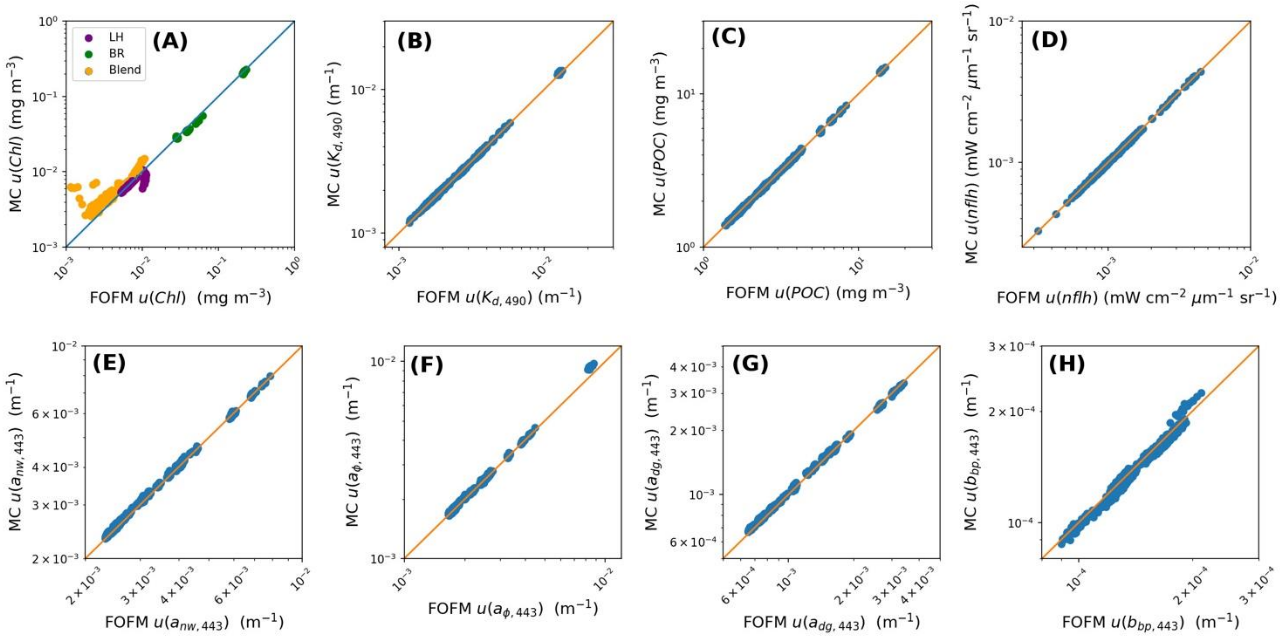

Figure 4: (A-D) histograms of derived Chl, $K_{d,490}$, POC, and nflh, respectively. (E-H) histograms of FOFM-estimated uncertainties in derived Chl, $K_{d,490}$, POC, and nflh, respectively computed using 5% spectrally flat, uncorrelated uncertainty in input R_{rs}. (I-L) histograms of FOFM-estimated relative uncertainties in derived Chl, $K_{d,490}$, POC, and nflh, respectively. Note: FOFM-estimates of POC relative uncertainties in this example was invariant. Dashed curves represent MC results, solid blue bars represent FOFM results

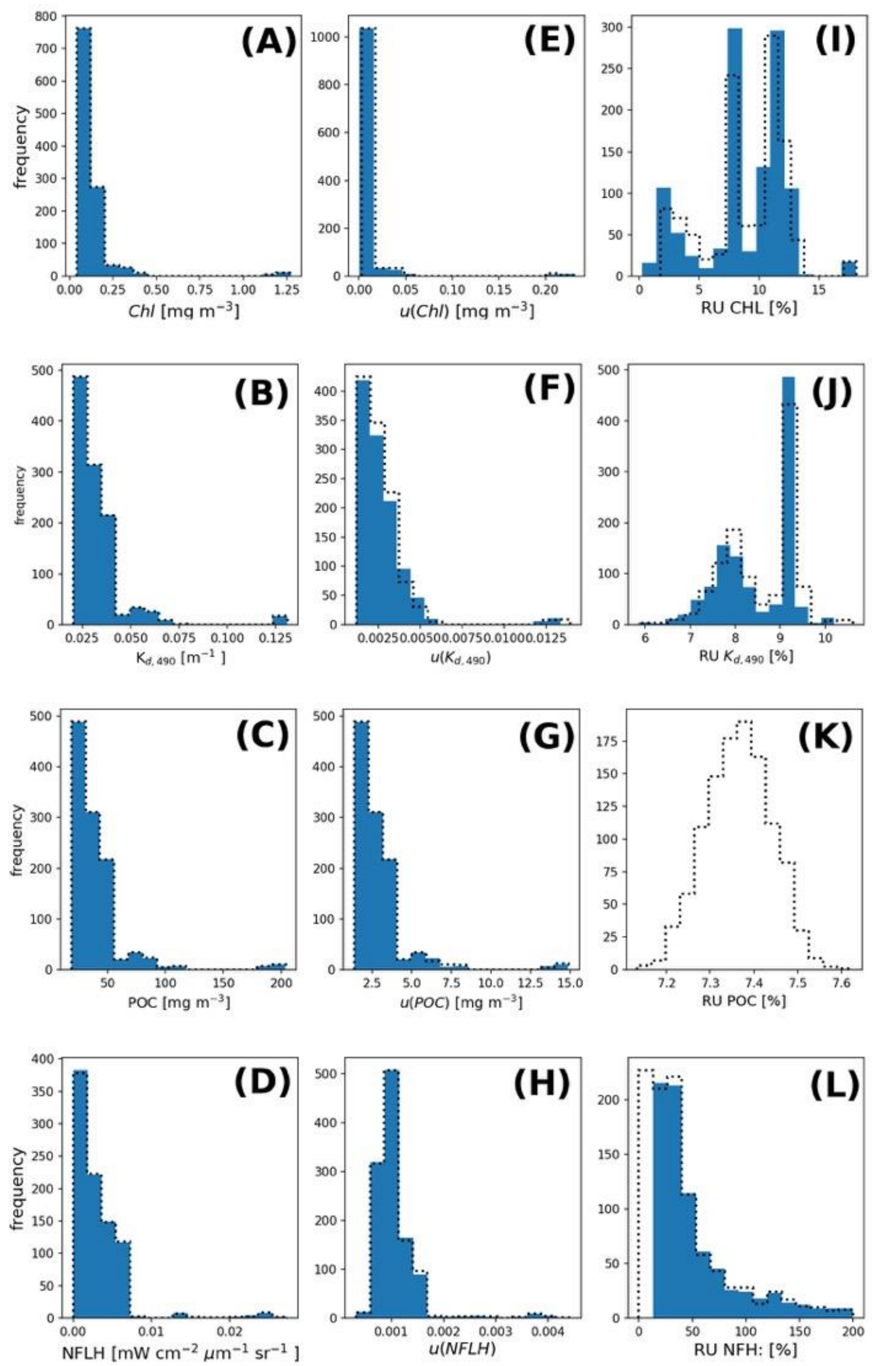

Figure 5: (A-D) histograms of derived $a_{nw,443}$, $a_{dg,443}$, $a_{\phi,443}$, and $b_{bp,443}$, respectively. (E-H) histograms of FOFM-estimated uncertainties in derived $a_{nw,443}$, $a_{dg,443}$, $a_{\phi,443}$, and $b_{bp,443}$, respectively computed using 5% spectrally flat, uncorrelated uncertainty in input R_{rs}.. (I-L) histograms of FOFM-estimated relative uncertainties in derived $a_{nw.443}$, $a_{dg,443}$, $a_{\phi,443}$, and $b_{bp,443}$, respectively. Dashed curves represent MC results, solid blue bars represent FOFM results.

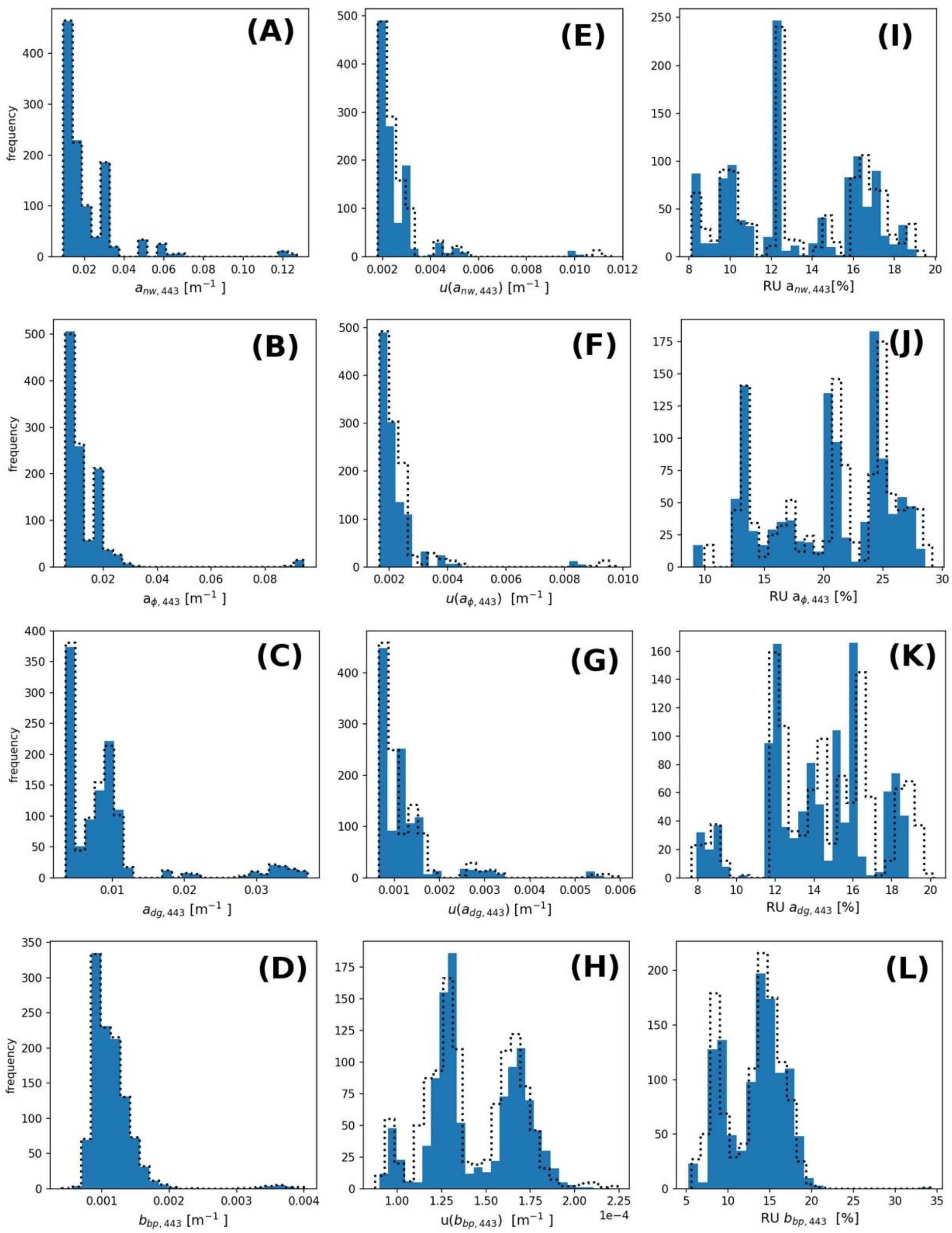

Figure 6: Upper row are histograms of derived OC data products uncertainties estimated using the FOFM method. Bottom row are histograms of derived IOP data product uncertainties estimated using the FOFM method. The four histograms in each subplot correspond to four different input u(R_{rs}): spectrally flat R_{rs} relative uncertainties of 1% (dashed black), 5% (blue) and 10% (orange) as well as spectrally dependent relative uncertainties taken from (Hu et al., 2013) outlined in green dashed line.

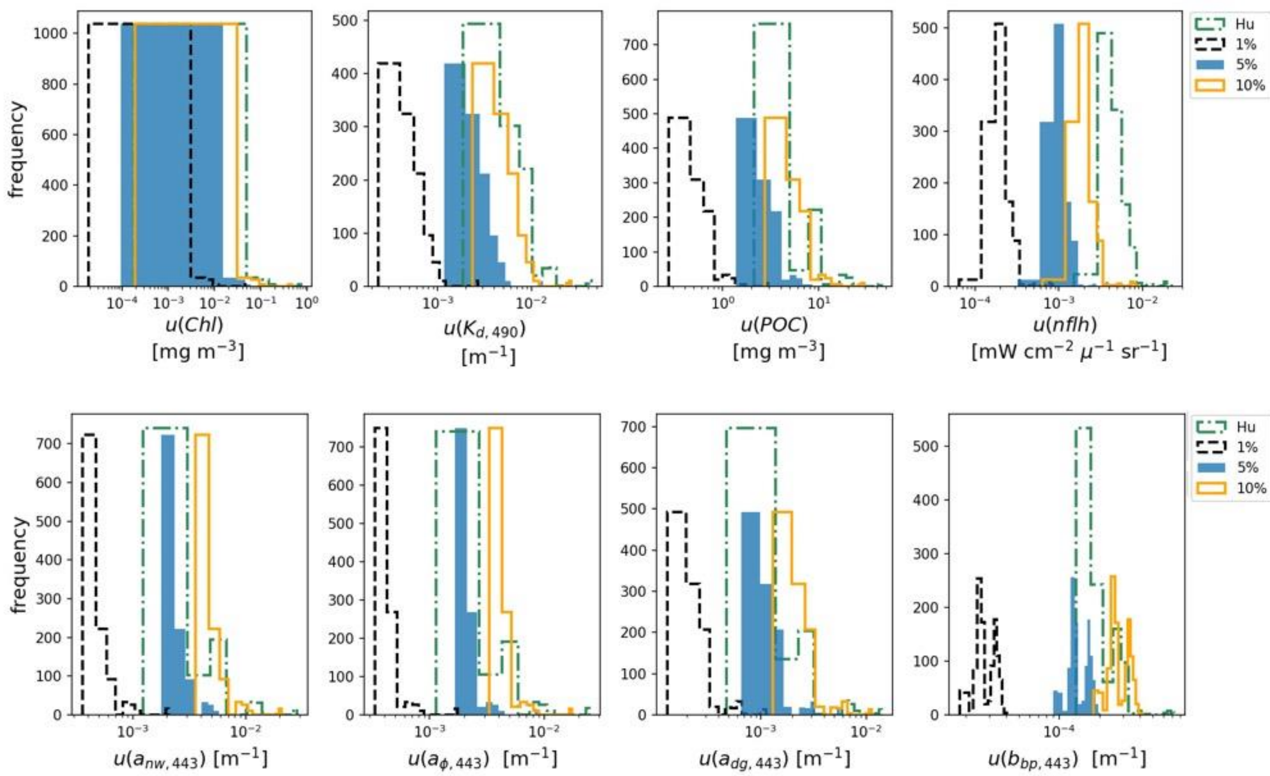

Figure 7: Derived data products for a SeaWiFS image of waters surrounding the Hawaii Islands captured on 1 December 2000. (a) Chl concentration derived using OCI algorithm, (b) u(Chl) computed with covariances included, (c) relative uncertainty in Chl computed with estimated R_{rs} covariances included, (d) u(Chl) calculated without estimated R_{rs} covariances included, and (e) relative uncertainty in Chl computed without estimated R_{rs} covariances included.

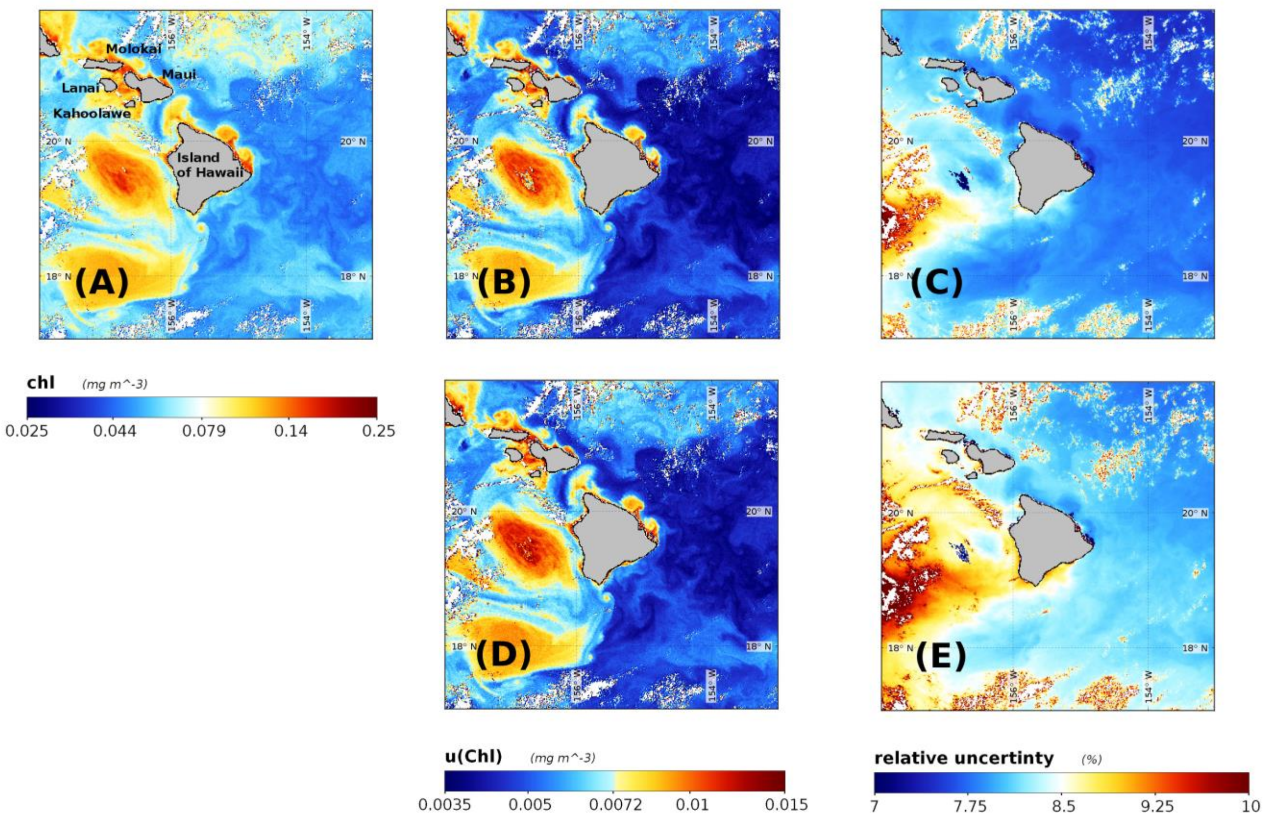

Figure 8: Pie charts demonstrate how individual uncertainty sources contribute to estimates of total measurement uncertainty. Here we consider: (A) a blue-green band-ratio POC algorithm and (B) an IOP-based POC algorithm. We note that these examples are intended to illustrate how one might visualize source contributions to measurement uncertainty. These plots are not intended for algorithm comparison purposes.

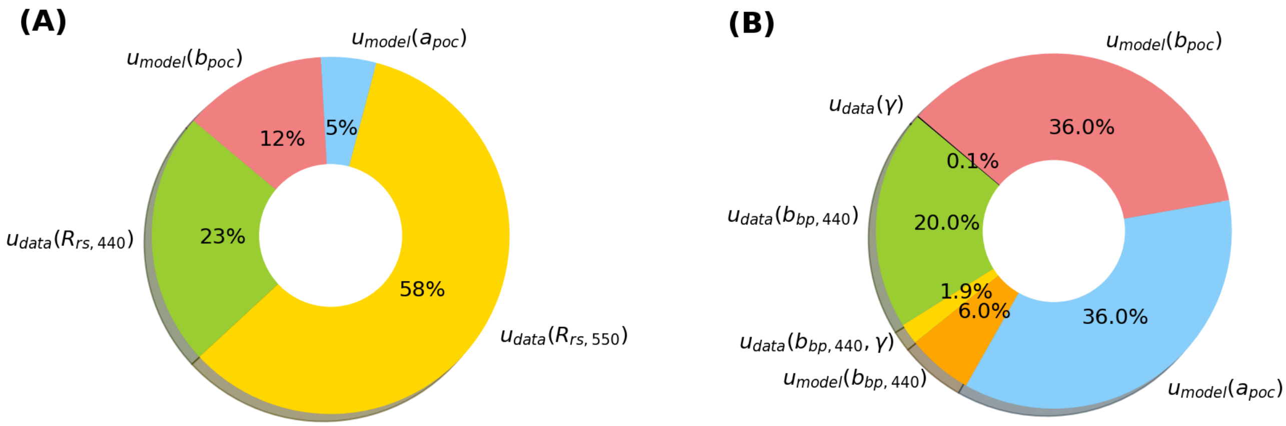

Appendix A: Chlorophyll concentration and uncertainty

NASA's standard chlorophyll-a pigment (*Chl*; mg m^{-3}) algorithm is a combination of a blue-to-green maximum band ratio algorithm (Chl_{BR}) (O'Reilly et al., 1998) and a chlorophyll index (line height) algorithm (Chl_{LH}) (Hu, Lee, et al., 2012). During pixel-by-pixel processing, both Chl_{BR} and Chl_{LH} are computed.

A.1 Band ratio Chl model

Chl_{BR} is returned as the solution when Chl_{BR} > 0.2 mg m^{-3} and is computed as follows:

$$Chl_{BR} = 10^{\alpha} \quad [A1]$$

which has the derivative:

$$\frac{\partial Chl_{BR}}{\partial \alpha} = \log(10)10^{\alpha} \quad [A2]$$

where α is a polynomial function. The order of the polynomial, $N=4$, and the coefficients a_i are sensor dependent. Specifically, α is expressed as:

$$\alpha = \sum_{i=1}^{4} a_i \left[LR \right]^i \quad [A3]$$

and has the derivative (assuming the coefficients, a_i, have no uncertainties):

$$\frac{\partial \alpha}{\partial LR} = \sum_{i=0}^{4} i a_i \left[LR \right]^{i-1} . \quad [A4]$$

The log-ratio, *LR*, term is:

$$LR = \log_{10}\left(\frac{R_{rs,b}}{R_{rs,g}} \right) \quad [A5]$$

where $R_{rs,b}$ and $R_{rs,g}$ are remote sensing reflectances centered on blue and green sensor bands, respectively.

The partial derivatives of Eq. A5 are:

$$\frac{\partial LR}{\partial R_{rs,b}} = \frac{1}{\log(10)} \frac{1}{R_{rs,g}} , \quad [A6a]$$

and

$$\frac{\partial LR}{\partial R_{rs,g}} = - \frac{1}{\log(10)} \frac{R_{rs,b}}{R_{rs,g}^2} . \quad [A6b]$$

In this analysis, we consider the Chl_{BR} formulation known as "OC4" tuned for the SeaWiFS sensor where the green reference band, λ_g, is centered on 555 nm and the blue band is selected as follows:

$$R_{rs,b} = \max\{R_{rs,443}, R_{rs,490}, R_{rs,510}\} \quad \text{[A7]}$$

The fourth order polynomial coefficients a_i were determined empirically from a comprehensive in situ data set of coincident *Chl* and $R_{rs}(\lambda)$ data *(Werdell & Bailey, 2005)*. For OC4, the coefficients a_0, a_1, a_2, a_3, a_4, have values of 0.3272, -2.9940, 2.7218, -1.2259, and -0.5683, respectively.

The variance in Chl_{BR} is thus estimated as:

$$u^2(Chl_{BR}) = \left(\frac{\partial Chl_{BR}}{\partial R_{rs,b}}\right)^2 u^2(R_{rs,b}) + \left(\frac{\partial Chl_{BR}}{\partial R_{rs,555}}\right)^2 u^2(R_{rs,g}) + 2\frac{\partial Chl_{BR}}{\partial R_{rs,b}}\frac{\partial Chl_{BR}}{\partial R_{rs,555}} u(R_{rs,b}, R_{rs,555}) \quad \text{[A8]}$$

where $u^2(R_{rs,b})$ and $u^2(R_{rs,555})$ are the variances of $R_{rs,b}$ and $R_{rs,555}$, respectively and the $u(R_{rs,b},R_{rs,555})$ is the error covariance of $R_{rs,b}$ and $R_{rs,555}$. The partial derivatives in Eq. A8 are computed as:

$$\frac{\partial Chl_{BR}}{\partial R_{rs,b}} = \frac{\partial Chl_{BR}}{\partial \alpha}\frac{\partial \alpha}{\partial LR}\frac{\partial LR}{\partial R_{rs,b}} \quad \text{[A9a]}$$

and

$$\frac{\partial Chl_{BR}}{\partial R_{rs,555}} = \frac{\partial Chl_{BR}}{\partial \alpha}\frac{\partial \alpha}{\partial LR}\frac{\partial LR}{\partial R_{rs,555}}\ . \quad \text{[A9b]}$$

A.2 Line height Chl model

Chl_{LH} is returned as the solution when $Chl_{LH} \leq 0.15$ mg m^{-3} and is computed as follows:

$$Chl_{LH} = 10^b, \quad \text{[A10]}$$

which has the derivative:

$$\frac{\partial Chl_{LH}}{\partial b} = \log(10)10^b, \quad \text{[A10]}$$

where,

$$b = -0.4909 + 191.5690\,LH \quad \text{[A11]}$$

which has the derivative:

$$\frac{\partial b}{\partial LH} = 191.6590\ . \quad \text{[A13]}$$

The *LH* term has the form:

$$LH = R_{rs,555} - \left[R_{rs,443} + \frac{(555 - 443)}{(670 - 443)} \left(R_{rs,670} - R_{rs,443} \right) \right]. \quad \text{[A14]}$$

with the following partial derivatives:

$$\frac{\partial LH}{\partial R_{rs,443}} = \frac{(555 - 443)}{(670 - 443)} - 1 , \quad \text{[A15a]}$$

$$\frac{\partial LH}{\partial R_{rs,555}} = 1, \quad \text{[A15b]}$$

and

$$\frac{\partial LH}{\partial R_{rs,670}} = - \frac{(555 - 443)}{(670 - 443)} . \quad \text{[A15c]}$$

The variance in Chl_{LH} can then be estimated as:

$$\begin{aligned} u^2(Chl_{LH}) = & \left(\frac{\partial Chl_{LH}}{\partial R_{rs,443}} \right)^2 u^2(R_{rs,443}) + \left(\frac{\partial Chl_{LH}}{\partial R_{rs,555}} \right)^2 u^2(R_{rs,555}) + \left(\frac{\partial Chl_{LH}}{\partial R_{rs,670}} \right)^2 u^2(R_{rs,670}) \\ & + 2 \frac{\partial Chl_{LH}}{\partial R_{rs,443}} \frac{\partial Chl_{LH}}{\partial R_{rs,555}} u(R_{rs,443}, R_{rs,555}) + 2 \frac{\partial Chl_{LH}}{\partial R_{rs,443}} \frac{\partial Chl_{LH}}{\partial R_{rs,670}} u(R_{rs,443}, R_{rs,670}) \\ & + 2 \frac{\partial Chl_{LH}}{\partial R_{rs,555}} \frac{\partial Chl_{LH}}{\partial R_{rs,670}} u(R_{rs555}, R_{rs,670}) \end{aligned} \quad \text{[A16]}$$

where $u^2(R_{rs,443})$, $u^2(R_{rs,555})$ and $u^2(R_{rs,670})$ are the variances of $R_{rs,443}$, $R_{rs,555}$, and $R_{rs,670}$, respectively. The term $u(R_{rs,443}, R_{rs,555})$ is the error covariance of $R_{rs,443}$ and $R_{rs,555}$, $u(R_{rs,443}, R_{rs,670})$ is the error covariance of $R_{rs,443}$ and $R_{rs,670}$, and $(R_{rs,555}, R_{rs,670})$ is the error covariance of $R_{rs,555}$, and $R_{rs,670}$. The partial derivatives in Eq. A16 are computed as:

$$\frac{\partial Chl_{LH}}{\partial R_{rs,443}} = \frac{\partial Chl_{LH}}{\partial \beta} \frac{\partial \beta}{\partial LH} \frac{\partial LH}{\partial R_{rs,443}} , \quad \text{[A17a]}$$

$$\frac{\partial Chl_{LH}}{\partial R_{rs,555}} = \frac{\partial Chl_{LH}}{\partial \beta} \frac{\partial \beta}{\partial LH} \frac{\partial LH}{\partial R_{rs,555}} , \quad \text{[A17b]}$$

and

$$\frac{\partial Chl_{LH}}{\partial R_{rs,670}} = \frac{\partial Chl_{LH}}{\partial \beta} \frac{\partial \beta}{\partial LH} \frac{\partial LH}{\partial R_{rs,670}} . \quad \text{[A17c]}$$

A.3 Blended Chl product

For intermediate conditions where $Chl_{LH} > 0.15$ mg m^{-3} and $Chl_{BR} \leq 0.2$ mg m^{-3}, Chl_{LH} and Chl_{BR} values are blended together and returned as the solution (Hu, Lee, et al., 2012). The blending is performed as follows:

$$Chl_{blend} = Chl_{LH}\frac{(0.20 - Chl_{LH})}{0.2 - 0.15} + Chl_{BR}\frac{(Chl_{LH} - 0.15)}{0.2 - 0.15}\ . \qquad \text{[A18]}$$

The variance in Chl_{blend} is estimated as follows:

$$\begin{aligned}
u^2(Chl_{blend}) = &\left(\frac{\partial Chl_{blend}}{\partial R_{rs,443}}\right)^2 u^2(R_{rs,443}) + \left(\frac{\partial Chl_{blend}}{\partial R_{rs,490}}\right)^2 u^2(R_{rs,490}) + \left(\frac{\partial Chl_{blend}}{\partial R_{rs,510}}\right)^2 u^2(R_{rs,510}) \\
&+ \left(\frac{\partial Chl_{blend}}{\partial R_{rs,555}}\right)^2 u^2(R_{rs,555}) + \left(\frac{\partial Chl_{blend}}{\partial R_{rs,670}}\right)^2 u^2(R_{rs,670}) \\
&+ 2\frac{\partial Chl_{blend}}{\partial R_{rs,443}}\frac{\partial Chl_{blend}}{\partial R_{rs,490}} u(R_{rr,443}, R_{rs,490}) + 2\frac{\partial Chl_{blend}}{\partial R_{rs,443}}\frac{\partial Chl_{blend}}{\partial R_{rs,510}} u(R_{rs,443}, R_{rs,510}) \\
&+ 2\frac{\partial Chl_{blend}}{\partial R_{rs,443}}\frac{\partial Chl_{blend}}{\partial R_{rs,555}} u(R_{rs,443}, R_{rs,555}) + 2\frac{\partial Chl_{blend}}{\partial R_{rs,443}}\frac{\partial Chl_{blend}}{\partial R_{rs670}} u(R_{rs,443}, R_{rs,670}) \\
&+ 2\frac{\partial Chl_{blend}}{\partial R_{rs,490}}\frac{\partial Chl_{blend}}{\partial R_{rs,510}} u(R_{rs,490}, R_{rs,510}) + 2\frac{\partial Chl_{blend}}{\partial R_{rs,490}}\frac{\partial Chl_{blend}}{\partial R_{rs,555}} u(R_{rs,490}, R_{rs,555}) \\
&+ 2\frac{\partial Chl_{blend}}{\partial R_{rs,490}}\frac{\partial Chl_{blend}}{\partial R_{rs,670}} u(R_{rs,490}, R_{rs,670}) + 2\frac{\partial Chl_{blend}}{\partial R_{rs,510}}\frac{\partial Chl_{blend}}{\partial R_{rs,555}} u(R_{rs,510}, R_{rs,555}) \\
&+ 2\frac{\partial Chl_{blend}}{\partial R_{rs,510}}\frac{\partial Chl_{blend}}{\partial R_{rs,670}} u(R_{rs,510}, R_{rs,670}) + 2\frac{\partial Chl_{blend}}{\partial R_{rs,555}}\frac{\partial Chl_{blend}}{\partial R_{rs670}} u(R_{rs,555}, R_{rs,670}).
\end{aligned} \qquad \text{[A19]}$$

Where $u^2(R_{rs,i})$ terms are variances and $u(R_{rs,i}, R_{rs,j})$ terms are error covariances. The partial derivatives in Equation A19 are:

$$\frac{\partial Chl_{blend}}{\partial R_{rs,i}} = \frac{1}{0.2 - 0.15}\left[0.2\frac{\partial Chl_{LH}}{\partial R_{rs,i}} - \frac{\partial Chl_{LH}^2}{\partial R_{rs,i}} + \frac{\partial(Chl_{BR}Chl_{LH})}{\partial R_{rs,i}} - 0.15\frac{\partial Chl_{BR}}{\partial R_{rs,i}}\right]. \qquad \text{[A20]}$$

and

$$\frac{\P Chl_{LH}^2}{\P R_{rs,i}} = 2Chl_{LH}\frac{\P Chl_{LH}}{\P R_{rs,i}}, \qquad \text{[A21a]}$$

$$\frac{\P(Chl_{LH}Chl_{BR})}{\P R_{rs,i}} = Chl_{LH}\frac{\P Chl_{BR}}{\P R_{rs,i}} + Chl_{BR}\frac{\P Chl_{LH}}{\P R_{rs,i}}. \qquad \text{[A21b]}$$

$$\frac{\P Chl_{LH}Chl_{BR}}{\P R_{rs,i}} = Chl_{LH}\frac{\P Chl_{BR}}{\P R_{rs,i}} + Chl_{BR}\frac{\P Chl_{LH}}{\P R_{rs,i}}$$

Appendix B: Diffuse attenuation coefficient and uncertainty

NASA's standard algorithm for the deriving diffuse attenuation coefficient at 490 nm, $K_{d,490}$ (m^{-1}), is based on blue-to-green reflectance ratios (Mueller, 2000). The algorithm was empirically developed using a high quality in situ dataset of coincident $K_d(490)$ and $R_{rs}(\lambda)$ data (Mueller, 2000; Werdell & Bailey, 2005) and is computed as follows:

$$K_{d,490} = 0.0166 + 10^{\chi} \qquad \text{[B1]}$$

which has the derivative with respect to χ of:

$$\frac{\partial K_{d,490}}{\partial \chi} = \log(10)10^{\chi} \qquad \text{[B2]}$$

where χ is a polynomial function. The order of the polynomial, $N=4$, and the coefficients b_i are sensor dependent. Specifically, χ is expressed as:

$$\chi = \sum_{i=0}^{4} b_i \left[LR \right]^i \qquad \text{[B3]}$$

and has the derivative (assuming the coefficients, b_i, have no uncertainties):

$$\frac{\partial \chi}{\partial LR} = \sum_{i=3}^{4} i b_i \left[LR \right]^{i-1} \ . \qquad \text{[b4]}$$

In this study, we consider the $K_{d,490}$ algorithm tuned for SeaWiFS such that the blue and green remote sensing reflectances, $R_{rs,b}$ and $R_{rs,g}$, that are centered on 490 nm and 555 nm, respectively. Also, the fourth order polynomial coefficients b_0, b_1, b_2, b_3, and b_4 are -0.8515, -1.8263, 1.8714, -2.4414, and -1.0690, respectively. Thus, the log-ratio, LR, term is:

$$LR = \log_{10}\left(\frac{R_{rs,490}}{R_{rs,555}} \right) \qquad \text{[B5]}$$

The partial derivatives of Eq. B5 are:

$$\frac{\partial LR}{\partial R_{rs,490}} = \frac{1}{\log(10)} \frac{1}{R_{rs,555}} \ , \qquad \text{[B6a]}$$

and

$$\frac{\partial LR}{\partial R_{rs,555}} = -\frac{1}{\log(10)} \frac{R_{rs,490}}{R_{rs,555}} \ . \qquad \text{[B6b]}$$

The variance in $K_{d,490}$ can thus be estimated as:

$$u^2(K_{d,490}) = \left(\frac{\partial K_{d,490}}{R_{rs,490}}\right)^2 u^2(R_{rs,490}) + \left(\frac{\partial K_{d,490}}{R_{rs,555}}\right)^2 u^2(R_{rs,555}) + 2\frac{\partial K_{d,490}}{R_{rs,490}}\frac{\partial K_{d,490}}{R_{rs,555}} u(R_{rs,490}, R_{rs,555}) \quad \text{[B8]}$$

where u($R_{rs,490}$) and u($R_{rs,555}$) are the variances of $R_{rs,490}$ and $R_{rs,555}$, respectively and u($R_{rs,490}$, $R_{rs,555}$) is the error covariance of $R_{rs,490}$ and $R_{rs,555}$. The partial derivatives in Eq. B8 are computed as:

$$\frac{\partial K_{d,490}}{\partial R_{rs,490}} = \frac{\partial K_{d,490}}{\partial \chi}\frac{\partial \chi}{\partial LR}\frac{\partial LR}{\partial R_{rs,490}} \quad \text{[B9a]}$$

and

$$\frac{\partial K_{d,490}}{\partial R_{rs,555}} = \frac{\partial K_{d,490}}{\partial \chi}\frac{\partial \chi}{\partial LR}\frac{\partial LR}{\partial R_{rs,555}} \; . \quad \text{[B9b]}$$

Appendix C: Particulate organic carbon

NASA's Particulate Organic Carbon (*POC*) algorithm as defined by Stramski et al. (2008a) computes near-surface particular organic carbon concentration (mg m^{-3}) as follows:

$$POC = a_{poc} BR^{b_{poc}} \quad \text{[C1]}$$

Where, a_{poc} and b_{poc} are constants with values of 203.2 and -1.034, respectively. The *BR* term is a blue-green reflectance ratio with the numerator and denominator being remote sensing reflectances centered on 443 and 555 nm, respectively.

$$BR = \frac{R_{rs,443}}{R_{rs,555}} \quad \text{[C2]}$$

The derivative of Equation C1 with respect to *BR* is:

$$\frac{\partial POC}{\partial BR} = a_{poc} b_{poc} BR^{(b_{poc} - 1)}., \quad \text{[C3]}$$

And Equation C2 had the following partial derivatives:

$$\frac{\partial BR}{\partial R_{rs,443}} = \frac{1}{R_{rs,555}} \;, \quad \text{[C4]}$$

and

$$\frac{\partial BR}{\partial R_{rs,555}} = - \frac{R_{rs,443}}{(R_{rs,555})^2} \;. \quad \text{[C5]}$$

The variance of *POC* is estimated as:

$$u^2(POC) = \left(\frac{\partial POC}{\partial R_{rs,443}}\right)^2 u^2(R_{rs,443}) + \left(\frac{\partial POC}{\partial R_{rs,555}}\right)^2 u^2(R_{rs,555}) + 2\frac{\partial POC}{\partial R_{rs,443}}\frac{\partial POC}{\partial R_{rs,555}} u(R_{rs,443}, R_{rs,555}) \quad \text{[C5]}$$

where $u^2(R_{rs,443})$ and $u^2(R_{rs,555})$ are variances of $R_{rs,443}$ and $R_{rs,555}$, respectively. $u(R_{rs,443},R_{rs,555})$ is the error covariance of $R_{rs,443}$ and $R_{rs,555}$. The partial derivatives in Eq. C5 are computed as:

$$\frac{\partial POC}{\partial R_{rs,443}} = \frac{\partial POC}{\partial BR}\frac{\partial BR}{\partial R_{rs,443}} \quad \text{[C6a]}$$

and

$$\frac{\partial POC}{\partial R_{rs,555}} = \frac{\partial POC}{\partial BR}\frac{\partial BR}{\partial R_{rs,555}} \quad \text{[C6b]}$$

Appendix D: Normalized fluorescent line height

NASA's algorithm for normalized fluorescence line height, *nflh* (mW cm^{-2} μm^{-1} sr^{-1}), is a measurement of chlorophyll fluorescence emission under natural sunlight (Behrenfeld et al., 2009). The algorithm uses spectral values of normalized water leaving radiances, *nLw*. Values of *nflh* are calculated as the difference between the observed nLw_{678} and a linearly interpolated nLw_{678} from two adjacent bands (nLw_{667} and nLw_{748}). Currently, the algorithm is implemented for MODIS only as:

$$nflh = nLw_{678} - nLw_{667}\left(\frac{70}{81}\right) - nLw_{748}\left(\frac{11}{81}\right) \qquad \text{[D1]}$$

We note that nLw_i is related to $R_{rs,i}$ as follows:

$$nLw_i = F_{0,i} R_{rs,i} \qquad \text{[D2]}$$

Where, $F_{0,i}$ is the spectral extraterrestrial solar irradiance (Thuillier et al., 2003).

The variance in *nflh* is estimated as (assuming that F_0 has no uncertainties):

$$\begin{aligned} u^2(nflh) = &\left(\frac{\partial nflh}{\partial R_{rs,667}}\right)^2 u^2(R_{rs,667}) + \left(\frac{\partial nflh}{\partial R_{rs,678}}\right)^2 u^2(R_{rs,678}) + \left(\frac{\partial nflh}{\partial R_{rs,748}}\right)^2 u^2(R_{rs,748}) \\ &+ 2\frac{\partial nflh}{\partial R_{rs,667}}\frac{\partial nflh}{\partial R_{rs,678}} u(R_{rs,667}, R_{rs,678}) + 2\frac{\partial nflh}{\partial R_{rs,667}}\frac{\partial nflh}{\partial R_{rs,748}} u(R_{rs,667}, R_{rs,748}) \\ &+ 2\frac{\partial nflh}{\partial R_{rs,678}}\frac{\partial nflh}{\partial R_{rs,748}} u(R_{rs,678}, R_{rs,748}) \end{aligned} \qquad \text{[D3]}$$

where $u(R_{rs,667})$, $u(R_{rs,678})$, and $u(R_{rs,748})$ are the uncertainties in $R_{rs,667}$, $R_{rs,678}$, and $R_{rs,748}$, respectively. The term $u(R_{rs,667}, R_{rs,678})$ is the error covariance of $R_{rs,667}$ and $R_{rs,678}$, $u(R_{rs,667}, R_{rs,748})$ is the error covariance of $R_{rs,667}$ and $R_{rs,748}$, and $(R_{rs,678}, R_{rs,748})$ is the error covariance of $R_{rs,667}$, and $R_{rs,748}$. The partial derivatives in Eq. D3 are:

$$\frac{\partial nflh}{\partial R_{rs,667}} = -\left(\frac{70}{81}\right) F_{0,667}\ , \qquad \text{[D4a]}$$

$$\frac{\partial nflh}{\partial R_{rs,678}} = F_{0,678}\ , \qquad \text{[D4b]}$$

and

$$\frac{\partial nflh}{\partial R_{rs,748}} = -\left(\frac{11}{81}\right) F_{0,748}\ . \qquad \text{[D4c]}$$

Appendix E: Inherent optical properties

The Generalized Inherent Optical Properties (GIOP) is a semianalytical algorithm used to derive standard IOP data products as distributed by NASA's OB.DAAC. Comprehensive discussion of the GIOP can be found elsewhere (Franz & Werdell, 2010; McKinna et al., 2016; Werdell et al., 2013), however, below we briefly overview the algorithm.

E.1 The forward model

At the core of the GIOP is a forward reflectance model that simulates the spectral sub-surface remote-sensing reflectance, $r_{rs,i}$, as a function of the water-column's inherent optical properties (IOPs). The default configuration of the GIOP uses the quasi-single scattering approximation of Gordon et al. (1988) to model the subsurface spectral remote-sensing reflectance, $r_{rs,i}^{\mathrm{mod}}$, as a function of IOPs:

$$r_{rs,i}^{\mathrm{mod}} = g_0 u_i + g_1 u_i^2 \qquad \text{[E1]}$$

and

$$u_i = \frac{b_{b,i}}{a_i + b_{b,i}} \qquad \text{[E2]}$$

where, a_i is the total spectral absorption coefficient, $b_{b,i}$ is the total spectral backscattering coefficient, and g_0 and g_1 are constants with default values of 0.0949 and 0.0794, respectively. The coefficient a_i can be expressed as the sum of absorbing constituent matter present:

$$a_i = a_{w,i} + x_f a_{f,i}^{*} + x_{dg} a_{dg,i}^{*} \qquad \text{[E3]}$$

where, the $a_{w,i}$ is the spectral absorption coefficient of pure water. The two remaining spectral absorption coefficient terms on the right-hand side of Equation E3 are expressed as a product of a normalized spectral absorption coefficient ($a*$) and its magnitude (x). The subscripts ϕ, and dg denote the constituents phytoplankton and colored dissolved and detrital matter, respectively. Similarly, $b_{b,i}$ can be expressed as:

$$b_{b,i} = b_{bw,i} + x_p b_{bp,i}^{*} \qquad \text{[E4]}$$

where the subcomponents of water and particulate matter are denoted by the subscripts w and p. Because pure water IOPs and the spectral shapes of other constituent matter can be parameterized at runtime, $r_{rs,i}^{\mathrm{mod}}$ becomes a function of three free variables:

$$r_{rs,i}^{\mathrm{mod}} = f(x_f, x_{dg}, x_p) \qquad \text{[E5]}$$

A mathematical solution method (default: non-linear least squares optimization) is then employed to find the optimal set of x_φ, x_{dg}, and x_p such that $r_{rs,i}^{\mathrm{mod}}$ best matches the sensor-observed sub-surface remote-sensing reflectance, $r_{rs,i}^{\mathrm{mod}}$. A "best match" is achieved once some distance metric (e.g. chi-squared) falls below a predefined threshold. We note that $r_{rs,i}^{\mathrm{mod}}$ is computed from above-water remote sensing reflectance, $R_{rs,i}$ according to Lee et al. (Lee et al., 2002):

$$r_{rs,i}^{obs} = \frac{R_{rs,i}}{0.52 + 1.7 R_{rs,i}} \; . \qquad \text{[E6]}$$

Importantly, the GIOP's structure can be varied at runtime to assign the forward reflectance model, the normalized shapes of the IOP subcomponents ($a_{f,i}^{*}$, $a_{dg,i}^{*}$ and $b_{bp,i}^{*}$), and the mathematical solution method. We note that the spectral shape coefficients are normalized at 443 nm.

E.2 Bio-optical models

In the GIOP, the normalized shape components $a_{f,i}^{*}$, $a_{dg,i}^{*}$ and $b_{bp,i}^{*}$ are parameterized on a per-pixel basis using bio-optical models. Below we briefly describe the bio-optical models used in the default configuration of the GIOP.

The spectral shape $a_{f,i}^{*}$ is modeled per-pixel using the methodology of Bricaud et al. (1998). Specifically, $a_{f,i}^{*}$ is a function of *Chl* as derived in Appendix A and the spectral vectors A_i and B_i:

$$a_{f,i}^{*} = \frac{0.055}{t} A_i Chl^{B_i - 1} \qquad \text{[E7]}$$

where, the scaling coefficient is:

$$t = A_{440} Chl^{B_{440} - 1} \qquad \text{[E8]}$$

The subscript 440 denotes that the scaling coefficient is computed at or near 440 nm. The resulting $a_{f,i}^{*}$ is chlorophyll-specific, hence the scaling factor x_{ϕ} has the physical value of chlorophyll concentration (Chl_{giop}). The spectral shape $a_{dg,i}^{*}$ is modeled using an exponential function of the form:

$$a_{dg,i}^{*} = \exp\left\{ -S_{dg}(i - 440) \right\} \qquad \text{[E9}\}$$

where, S_{dg} is treated as a constant with a default value of 0.0183 sr^{-1} (Werdell et al., 2013). The normalized spectral shape has a value of 1.0 at or near 440 nm. Accordingly, the scaling factor x_{dg} is equivalent to $a_{dg,440}$.

The normalized particulate backscattering coefficient, $b_{bp,i}^{*}$, is modeled per-pixel using a power law:

$$b_{bp,i}^{*} = \left(\frac{440}{i} \right)^{g} \qquad \text{[E10]}$$

The normalized spectral shape has a value of 1.0 at or near 440 nm. The power law exponent, g, is calculated following Lee et al. (2002):

$$g = 2.0 - 2.4 e^{n} \qquad \text{[E11]}$$

where

$$n = -0.9\left(\frac{r_{rs,440}}{r_{rs,550}}\right) \quad \text{[E12]}$$

and $r_{rs,550}$ is centered on or near 550 nm.

E.3 Inverse solution method

The GIOP has a number of built-in inverse solution (spectral matching) methods that an end-user can select at runtime, these including: Levenberg-Marquardt (LM) optimization, Nelder-Mead (amoeba) optimization, and linear matrix inversion (LMI). In this study, we have chosen to use a LM solution method as is it is the current default in NASA's implementation of GIOP. The cost function is an Chi-squared sum of squares metric. When computing the Chi-squared metric, the following $R_{rs,i}$ bands were included: 412, 425, 443, 460, 475, 490, 510, 532, 555, 583, 617, 640, 655, 665 nm.

E.4 Uncertainty propagation

For non-linear least squares, the variance-covariance matrix of derived best-fit parameters, $\mathbf{V_x}$, can be estimated using the Jacobian matrix, $\mathbf{J}$, and the variance-covariance matrix of model inputs, $\mathbf{V_{rrs}}$ as:

$$\mathbf{V}_x = \mathbf{J}^{-1}\mathbf{V}_{\mathbf{r_{rs}}}(\mathbf{J}^{\mathrm{T}})^{-1}\,. \quad \text{[E13]}$$

For the GIOP, the uncertainties of x_ϕ, x_{dg}, and x_p can thus be estimated as the square root of the diagonal elements of $\mathbf{V_x}$. The matrix $\mathbf{V}_{\mathbf{r_{rs}}}$ is the variance-covariance matrix of r_{rs}. The matrix $\mathbf{J}$ is computed as:

$$\mathbf{J} = \begin{bmatrix} \frac{\partial r_{rs,i}}{\partial x_f} & \frac{\partial r_{rs,i}}{\partial x_{dg}} & \frac{\partial r_{rs,i}}{\partial x_p} \end{bmatrix} \quad \text{[E14]}$$

where the i^{th} wavelength element of each column can be expressed as:

$$\frac{\partial r_{rs,i}}{\partial x_f} = \frac{-[g_0 + 2g_1u_i][b_{b,i}a^*_{f,i}]}{[b_{b,i} + a_i]^2}\ , \quad \text{[E15a]}$$

$$\frac{\partial r_{rs,i}}{\partial x_{dg}} = \frac{-[g_0 + 2g_1u_i][b_{b,i}a^*_{dg,i}]}{[b_{b,i} + a_i]^2}\ , \quad \text{[E15b]}$$

and

$$\frac{\partial r_{rs,i}}{\partial x_p} = \frac{[g_0 + 2g_1u_i][a_ib^*_{bp,i}]}{[b_{b,i} + a_i]^2}\ . \quad \text{[E15c]}$$

The diagonal elements of $\mathbf{V}_{\mathbf{r_{rs}}}$ are equal to the square of uncertainties in sensor-observed sub-surface remote sensing reflectances, $u^2(r_{rs,i})$, and the off-diagonal elements of $\mathbf{V}_{\mathbf{r_{rs}}}$, $u(r_{rs,i}, r_{rs,j})$, are the covariances between $r_{rs,i}$ and $r_{rs,j}$. The elements $u^2(r_{rs,i})$ are computed as:

$$u^2(r_{rs,i}) = \left(\frac{\partial r_{rs,i}}{\partial R_{rs,i}}\right)^2 u^2(R_{rs,i}) \qquad \text{[E16]}$$

and the off-diagonal can be computed as:

$$u(r_{rs,i}, r_{rs,j}) = \frac{\partial r_{rs,i}}{\partial R_{rs,i}} \frac{\partial r_{rs,i}}{\partial R_{rs,j}} u(R_{rs,i}, R_{rs,j}) \qquad \text{[E17]}$$

where, $u(R_{rs,i}, R_{rs,j})$ is the covariance (if known) of above-water remote sensing reflectances $R_{rs,i}$ and $R_{rs,j}$. The partial derivative term in E16 is:

$$\frac{\partial r_{rs,i}}{\partial R_{rs,i}} = \frac{0.52}{\left[0.52 + 1.7 R_{rs,i}\right]^2} \;. \qquad \text{[E18]}$$

We note that for the approximation of $u(x_\phi)$, $u(x_{dg})$ and $u(x_p)$, computed from Eq. E13, the spectral shapes coefficients $a^*_{f,i}$, $a^*_{dg,i}$, and $b^*_{bp,i}$ are treated as uncertainty free. In practice, however, we note that $a^*_{f,i}$ and $b^*_{bp,i}$ have inherent uncertainties due to their dependence of *Chl* and $R_{rs,i}$, respectively. We remind the reader that in this study we have focused on propagation of data (radiometric) uncertainties and not on the impact of model (spectral shape) uncertainties. We have nonetheless still included relevant FOFM uncertainty formulations for spectral shape models in the following section.

E.5 Uncertainty in spectral shapes

For $b^*_{bp,i}$, variance of the spectral shape, $u^2(b^*_{bp,i})$, is driven by variance in the power law exponent, $u^2(\gamma)$, which can be computed as:

$$u^2(\gamma) = \left(\frac{\partial \gamma}{\partial r_{rs,440}}\right)^2 u^2(r_{rs,440}) + \left(\frac{\partial \gamma}{\partial r_{rs,550}}\right)^2 u^2(r_{rs,550}) + 2\frac{\partial \gamma}{\partial r_{rs,440}} \frac{\partial \gamma}{\partial r_{rs,550}} u(r_{rs,440}, r_{rs,550}). \qquad \text{[E19]}$$

The partial derivatives in Eq. E19 have the following form:

$$\frac{\partial \gamma}{\partial r_{rs,440}} = \frac{\partial \gamma}{\partial \nu} \frac{\partial \nu}{\partial r_{rs,440}} \qquad \text{[E20a]}$$

$$\frac{\partial \gamma}{\partial r_{rs,550}} = \frac{\partial \gamma}{\partial \nu} \frac{\partial \nu}{\partial r_{rs,550}} \qquad \text{[E20b]}$$

where,

$$\frac{\partial \gamma}{\partial \nu} = -2.4 e^{\nu} \;, \qquad \text{[E21]}$$

$$\frac{\partial \nu}{\partial r_{rs,440}} = -\frac{0.9}{r_{rs,440}} \;, \qquad \text{[E22]}$$

and

$$\frac{\partial \eta}{\partial r_{rs,550}} = 0.9\frac{r_{rs,440}}{(r_{rs,555})^2}. \quad \text{[E23]}$$

Finally, $u(b^*_{bp,i})$ is computed as:

$$u(b^*_{bp,i}) = u(\gamma)\log\left(\frac{440}{\lambda}\right)\left(\frac{440}{\lambda}\right)^{\gamma} \quad \text{[E24]}$$

and spectral uncertainty in the derived backscattering coefficient, $u(b_{bp,i})$, is:

$$u^2(b_{bp,i}) = \left(x_p u(b^*_{bp,i})\right)^2 + \left(b^*_{bp,i} u(x_p)\right)^2 + 2x_p b^*_{bp,i} u(x_p, b^*_{bp,i}) \quad \text{[E25]}$$

where the term $u(x_p, b^*_{bp,i})$ is the covariance between x_p and $b^*_{bp,i}$. When estimating $u(b_{bp,443})$ the first and third term in the right-hand side of E25 reduces to zero as $b^*_{bp,443}$ has a constant value of 1.0 and thus no variance, hence $u(x_p, b^*_{bp,443})$ is zero. We have not estimated/parameterized $u(x_p, b^*_{bp,i})$ in this study.

For $a^*_{\phi,i}$, uncertainty of the spectral shape, $u^2(a^*_{\phi,i})$, is driven by $u^2(Chl)$ and is computed as:

$$u^2(a^*_{\phi,i}) = \left(\frac{\partial a^*_{\phi}(\lambda)}{\partial Chl}\right)^2 u^2(Chl) \quad \text{[E26]}$$

where,

$$\frac{\partial a^*_{\phi,i}}{\partial Chl} = \frac{0.055}{\tau}\frac{\partial A_i Chl^{B_i-1}}{\partial Chl} + A_i Chl^{B_i-1}\frac{\partial}{\partial Chl}\left(\frac{0.055}{\tau}\right). \quad \text{[E27]}$$

The term in Eq. E27 are expressed as:

$$\frac{\partial A_i Chl^{B_i-1}}{\partial Chl} = \left[E_i - 1\right] A_i Chl^{B_i-2} \quad \text{[E28]}$$

and

$$\frac{\partial}{\partial Chl}\frac{0.055}{\tau} = \frac{\partial}{\partial Chl}\frac{0.055}{A_{440}Chl^{B_{440}-1}} = \frac{0.055\left[-B_{440}+1\right]}{A_{440}Chl^{B_{440}}}. \quad \text{[E29]}$$

Spectral variance in the derived phytoplankton absorption coefficient, $u^2(a_{\phi,i})$, is:

$$u^2(a_{f,i}) = \left(x_f u(a^*_{f,i})\right)^2 + \left(a^*_{f,i} u(x_f)\right)^2 + 2x_f a^*_{f,i} u(x_f, a^*_{f,i}) \ . \qquad [E30]$$

where the term $u(x_f, a^*_{f,i})$is the covariance between x_ϕ and $a^*_{f,i}$. When estimating $u(a_{\phi,443})$ the first and third terms in the right-hand side of E30 reduces to zero as $a^*_{f,443}$ has a constant value of 0.055 m^2 mg^{-1} and thus no variance, hence $u(x_f, a^*_{f,i})$ is zero. We have not estimated/parameterized $u(x_f, a^*_{f,i})$ in this study. We also note the spectral coefficients *A* and *B* and the scaling constant 0.055 each would have asscociated uncertainties, however, quanitifying these model coefficient ucertainties was beyond the scope of this work.

The spectral variance in the absorption coefficient of colored dissolved and detrital matter, $u^2(a_{dg,i})$, can be estimated as:

$$u^2(a_{dg,i}) = \left(a^*_{dg,i} u(x_{dg})\right)^2 + \left(x_{dg} u(a^*_{dg,i})\right)^2 + 2x_{dg} a^*_{dg,i} u(x_{dg}, a^*_{dg,i}) \ . \qquad [E31]$$

We note that in the default parametrization of the GIOP, S_{dg} is treated as a constant, thus there is no variance in $a^*_{dg,i}$, and the first and last terms therefore reduce to zero.

Appendix F: Approximating correlated uncertainties due to sensor noise

For this study, we have statistically estimated the spectral covariance matrix for SeaWiFS remote sensing reflectances $\mathbf{V}_{Rrs}$ due to radiometric uncertainty in L_t. The objective was to appraise the impact of spectral covariance terms in the analytical FOFM uncertainty framework, not to exactly quantify the covariances for any given sensor. We accept that it does not encompass a wide variety of viewing geometries, scan angles, water types, and aerosol conditions. In addition, we have not considered the uncertainties in ancillary datasets such ozone concentration, and wind speed. This methodology followed two steps: (i) statistically derive $\mathbf{V}_{Rrs}$ from a number of SeaWiFS images captured over the South Pacific Gyre, and (ii) numerically estimate the Jacobian matrix, $\mathbf{J}_{\mathbf{Lt}}$, describing how small changes in L_t affect derived R_{rs}. The SPG was selected as atmospheric and oceanic gradients in this region can be considered quasi-homogenous at local horizontal scales, thus local variability in $L_{t,i}$ can, to a first order, be attributed to sensor noise. We have used SeaWiFS MLAC data distributed by NASA's Ocean Biology Distributed Active Archive and Center (OB.DAAC) and processed these using NASA's l2gen code which is distributed as part of the SeaDAS data processing and visualization software package (https://seadas.gsfc.nasa.gov/). Following JCGM (2008) we have applied correction factors, including vicarious calibration and temporal degradation gains, in an attempt to reduce systematic effects.

First, we followed a similar approach to Lamquin et al. (2013) to statistically estimate the covariance matrix of top-of-atmosphere radiances, $\mathbf{V}_{Lt}$. A selection of 1,928 SeaWiFS MLAC level-1 files spanning the years 1999 – 2010 were processed using l2gen. Each L1 MLAC file was encompassed, in part or whole, a 1° x 1° region centered on 26°S, 122°E in the SPG. The derived level-2 (L2) data products were: $L_{t,i}$, $R_{rs,i}$ and *Chl*. The quality of each level-2 file was then assessed by examining the proportion of a file flagged as: CLDICE, HIGLINT, or PRODFAIL (probable cloud or ice contamination, sunglint: reflectance exceeds threshold, and failure in any product, respectively). This reduced the number of L2 files to 188. Next for each of the 188 L2 SPG extract files were manually inspected in SeaDAS v7.5, and depending on their size, one-to-three 5x5 pixel subsets were extracted where *Chl* and $R_{rs,510}$ appeared to be quasi-homogenous, resulting in a total of 212 L2 5x5-pixel subset files. Finally, the covariance matrix of L_t was computed for each 5x5 pixel subset from which a median average $\mathbf{V}_{Lt}$ was generated. Using $\mathbf{V}_{Lt}$ the correlation matrix $\mathbf{R}_{Lt}$ was then computed. Figure F1 shows estimated $\mathbf{V}_{Lt}$ and $\mathbf{R}_{Lt}$.

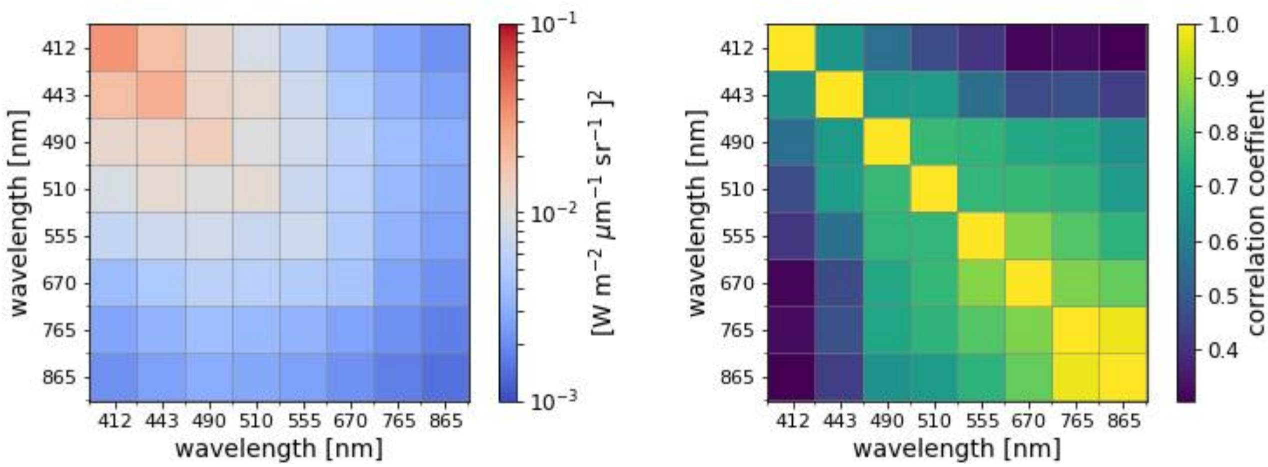

Figure F1: Left-hand side: estimated variance-covariance matrix of SeaWiFS top-of-atmosphere radiances, $\mathbf{V}_{Lt}$. Right-hand side: estimated correlation matrix of SeaWiFS top-of-atmosphere radiances, $\mathbf{R}_{Lt}$.

In this study, we approximated the per band top-of-atmosphere radiance uncertainty $u(L_{t,i})$ as 0.5% of total $L_{t,i}$:

$$u_n(L_{t,i}) = 0.005 \times L_{t,i}. \qquad [F2]$$

Next, we estimate a scaled top-of-atmosphere covariance matrix, $\mathbf{V}'_{Lt}$, on a pixel-by-pixel basis which has diagonal elements of $u^2(L_{t,i})$ and can be computed as:

$$\mathbf{V}'_{Lt} = \mathbf{S}\mathbf{R}_{Lt}\mathbf{S}, \qquad [F3]$$

where the matrix **S** is a diagonal matrix with elements equal to $1/u_n(L_{t,i})$.

A comprehensive method to propagate radiometric uncertainties through NASA's standard atmospheric correction algorithm was beyond the scope of this study. We instead used a numerical approach to approximate the covariance matrix of sensor-derived remote sensing reflectances, $\mathbf{V}_{Rrs}$. We first numerically estimated the Jacobian matrix, $\mathbf{J}_{Lt}$, or partial derivatives of $R_{rs,i}$ (412 – 670 nm) with respect to $L_{t,i}$ (412 – 865 nm)

$$\mathbf{J}_{Lt} = \begin{bmatrix} \frac{\partial R_{rs,412}}{\partial L_{t,412}}, & \frac{\partial R_{rs,412}}{\partial L_{t,443}}, & \cdots & \frac{\partial R_{rs,412}}{\partial L_{t,865}} \\ \frac{\partial R_{rs,443}}{\partial L_{t,412}}, & \frac{\partial R_{rs,443}}{\partial L_{t,443}}, & \cdots & \frac{\partial R_{rs443}}{\partial L_{t,865}} \\ \vdots & \vdots & & \vdots \\ \frac{\partial R_{rs,670}}{\partial L_{t412}}, & \frac{\partial R_{rs,670}}{\partial L_{t,443}}, & \cdots & \frac{\partial R_{rs,670}}{\partial L_{t,865}} \end{bmatrix}. \qquad [F4]$$

To generate $\mathbf{J}_{Lt}$, for the SeaWiFS MLAC image captured on 14 March 2007 and centered on the SPG, a subset of the image was extracted (25°S—27°S; 121.3°W -123.3°) with mean solar zenith angle (σ_{solz}) of 24.5° (1-σ_{solz}=0.69°) and mean sensor zenith angle (σ_{senz}) of 23.9° (1-σ_{senz}=1.9°). The subset was then processed using l2gen to derive $R_{rs,i}$ Next, the scene was reprocessed, however, this time $L_{t,412}$ was perturbed by a 0.1% of the average scene-wide value of $L_{t,412}$. The perturbation process was performed eight times, once for each spectral band. Finally, the partial derivatives in $\mathbf{J}_{Lt}$ were approximated numerically using a finite difference method, for example:

$$\frac{\partial R_{rs,443}}{\partial L_{t,443}} \approx \frac{R'_{rs,443} - R_{rs,443}}{\Delta L_{t,443}} \qquad [F5]$$

where, $R'_{rs,443}$ is the derived remote sensing reflectance at 443 derived when $L_{t,443}$ was perturbed by a small value $\Delta L_{t,443}$. Finally, $\mathbf{V}_{Rrs}$ can be estimated as:

$$\mathbf{V}_{Rrs} = \mathbf{J}_{Lt}\mathbf{V}'_{Lt}\mathbf{J}^T_{Lt}. \qquad [F6]$$

An example $\mathbf{V}_{Rrs}$ matrix and example of $u(R_{r,is})$ spectra are shown in Figure F2. These data were derived for the test SeaWiFS MLAC scene captured on 14 March 2007 over the SPG. All elements of $\mathbf{V}_{Rrs}$ are positive. We note that the estimated relative uncertainties (Figure F2) are of similar in shape and magnitude to those reported by Hu et al. (2013) for low-*Chl* waters.

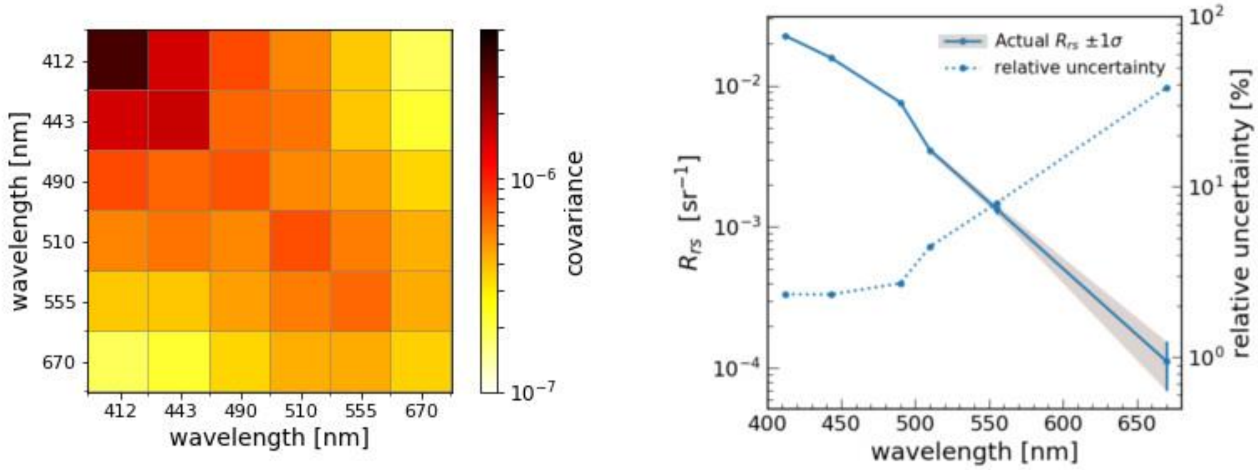

Figure F2: Left-hand side: estimated variance-covariance matrix of SeaWiFS remote sensing reflectances, V_{Rrs}, for a scene of the central SPG captured on 14 March 2007. Right-hand side: Solid blue line is depicting the average R_{rs} spectrum (log-scaled) for the SPG image with error bars that correspond to $u(R_{rs,i})$. Dashed line depicts relative uncertainty in R_{rs}.